

# General-Relativistic Lattice-Boltzmann Method for Radiation Transport

Tom Olsen,<sup>1,2</sup> and Luciano Rezzolla,<sup>2,1,3</sup>

<sup>1</sup>Frankfurt Institute for Advanced Studies, Ruth-Moufang-Str. 1, D-60438 Frankfurt, Germany

<sup>2</sup>Institut für Theoretische Physik, Goethe Universität, Max-von-Laue-Str. 1, 60438 Frankfurt am Main, Germany

<sup>3</sup>School of Mathematics, Trinity College, Dublin 2, Ireland

Accepted XXX. Received YYY; in original form ZZZ

## ABSTRACT

We present the first extension of the special-relativistic Lattice-Boltzmann Method for radiative transport developed by Weih et al. (2020c), to solve the radiative-transfer equation in curved spacetimes. The novel approach is based on the streaming of carefully selected photons along null geodesics and interpolating their final positions, velocities, and frequency shifts to all photons in a given velocity stencil. Furthermore, by transforming between the laboratory frame, the Eulerian frame, and the fluid frame, we are able to perform the collision step in the fluid frame, thus retaining the collision operator of the special-relativistic case with only minor modifications. As a result, with the new method we can model the evolution of the frequency-independent (“grey”) radiation field as it interacts with a background fluid via absorption, emission, and scattering in a curved background spacetime. Finally, by introducing a refined adaptive stencil, which is suitably distorted in the direction of propagation of the photon bundle, we can reduce the computational costs of the method while improving its performance in the optically-thin regime. A number of standard and novel tests are presented to validate the approach and exhibit its robustness and accuracy.

**Key words:** neutrinos – radiative transfer – scattering – methods:numerical – gravitation

## 1 INTRODUCTION

In essentially all observations of astronomical sources, the radiation that we receive is the result of a delicate and sometimes subtle interaction between the radiation field and the matter field that emits and absorbs it as it propagates. It is, therefore, of great importance that this interaction, which is mathematically described by the radiative-transfer equation (RTE). Given the nonlinear regimes normally encountered in astrophysical scenarios and the complexity of the radiative-transfer equation, the use of advanced numerical methods to tackle the radiative-transfer problem becomes inevitable. Such methods need to be combined with equally advanced approaches necessary to account for the dynamics of plasmas often encountered in astrophysics and modeled with the equations of magnetohydrodynamics (MHD). A perfect, but surely not unique example is the modelling of astrophysical compact objects as those involved in short gamma-ray bursts (Rezzolla et al. 2011; Palenzuela et al. 2013; Kiuchi et al. 2015), core-collapse supernovae (Mezzacappa et al. 2001; Just et al. 2015; O’Connor 2015; Kuroda et al. 2016), or in the merger of binary systems of neutron stars (BNS). In all of these scenarios, radiation fields composed of either photons or neutrinos, play a fundamental role in shaping the dynamics of the compact objects and, of course, in determining the astronomical observables (see, e.g., Ross-Wog et al. 2014; Siegel & Ciolfi 2016; Bovard et al. 2017; Dietrich & Ujevic 2017; Perego et al. 2017; Siegel & Metzger 2017; Fujibayashi et al. 2018; Fernández et al. 2019; Espino et al. 2024).

Several approaches are available in the literature for the inclusion of the effects of neutrinos in general-relativistic hydrodynamical or magnetohydrodynamical (GRMHD) simulations of BNS mergers. These range from very simple and computationally efficient “leakage-type” schemes (Ruffert et al. 1997; Galeazzi et al. 2013;

Most et al. 2019), where the local heating/cooling rates are directly estimated from the reaction cross-sections corrected with a diffusion prescription, over to the so-called “moment schemes”, where a varying number of moments of the Boltzmann equation for neutrinos is solved (Rezzolla & Miller 1994; Foucart et al. 2015; Just et al. 2015; Kuroda et al. 2016; Skinner et al. 2019; Melon Fuchsman & Mignone 2019; Weih et al. 2020b; Radice et al. 2022; Sun et al. 2022; Izquierdo et al. 2022). The most advanced approaches even consider the direct solution of the radiative transfer equation via MonteCarlo or other methods (Radice et al. 2013; Foucart et al. 2020; Roth et al. 2022; Izquierdo et al. 2024).

Among these different approaches, there is one that is closely related to the content of our work, the Lattice-Boltzmann method (LBM) for radiative transport recently developed by Weih et al. (2020c) within a special-relativistic context (SRLBM hereafter) and employed in BHAC (Porth et al. 2017; Olivares et al. 2019). The appealing aspects of this approach are its low computation cost and its high adaptability to optically intermediate and thick regimes. While it does not have issues with beam crossing, like the M1 scheme (Weih et al. 2020b; Musolino & Rezzolla 2024; Izquierdo et al. 2024), its performance is less accurate in optically thin regimes. More importantly, the method was developed for flat spacetime and, therefore, is not applicable in some of the most interesting scenarios described by GRMHD simulations of astrophysical compact objects.

Given these prospects and limitations, we here present the first implementation of the LBM for the solution of the general-relativistic RTE in curved background spacetimes. The core of our approach is based on the attempt to retain as much as possible of the logic of the SRLBM while adapting to the more complex background geometry. Since in LBM schemes “external forces” are either treated

arXiv:2502.17552v1 [gr-qc] 24 Feb 2025

as additional extra terms in the collision operator or by altering the streaming step, we follow the latter approach, as it is far more natural in a general-relativistic context. In particular, during the streaming step, we solve only certain null geodesics and interpolate the final photon positions, velocities, and frequencies to the photons in our LBM velocity stencil with the help of Fourier-transformations and spherical harmonics. In the collision step, on the other hand, we retain the collision operator in its special-relativistic form by transforming between multiple frames and carefully adapting the definition of the discretized intensities.

Our paper is structured as follows: Sec. 2 presents the basic mathematical aspects of the LBM, the 3 + 1 split of spacetime, and the geodesic equation in 3 + 1 form we employ. In Sec. 3, we review the recap the SRLBM as this will be useful in Sec. 4, where we illustrate the details of the GRLBM. In Sec. 4.2, we discuss the numerical methods we implemented to employ the GRLBM, while in Sec. 5 we present a long series of standard and novel tests to validate the robustness and accuracy of our approach. Finally, conclusions and future prospects of the LBM in general are presented in Sec. 6. Hereafter, we will adopt the  $(-, +, +, +)$  signature and assume Greek indices to run from 0 to 4, and Latin indices from 1 to 3.

## 2 MATHEMATICAL SETUP

### 2.1 The Lattice-Boltzmann Method

We recall that the LBM represent a numerical approach to model the dynamics of fluids on a mesoscopic scale rather than on a macroscopic one [Higuera et al. \(1989\)](#); [Succi \(2001\)](#). Thus, the starting point is the classical Boltzmann equation (see, e.g., [Rezzolla & Zanotti 2013](#))

$$\frac{df(\vec{x}, \vec{u}, t)}{dt} = \partial_t f + \vec{u} \cdot \vec{\nabla}_{\vec{x}} f + \frac{\vec{F}}{\rho} \cdot \vec{\nabla}_{\vec{u}} f = \Gamma[f], \quad (1)$$

where  $\vec{x}$  and  $\vec{u}$  are the position and velocity of a fluid particle at time  $t$ , respectively,  $\vec{F}$  is the force acting on the fluid, and  $\rho$  is the fluid density. The collision operator  $\Gamma[f]$  accounts for the interactions between the particles and is responsible for the relaxation of the distribution function  $f$  to the local equilibrium distribution function  $f^{\text{eq}}$ .

Solving this set of partial differential equations is complicated by the intrinsic seven-dimensionality and so it is convenient to retain the total differential on the left-hand side and to integrate it directly in time over an interval  $\Delta t = t_{n+1} - t_n$

$$\int_{t_n}^{t_{n+1}} \frac{df(\vec{x}, \vec{u}, t)}{dt} dt = \int_{t_n}^{t_{n+1}} \Gamma[f] dt. \quad (2)$$

The left-hand side of Eq. (2) can be integrated exactly, while the right-hand side is approximated with a numerical integral, assuming the collision operator  $\Gamma[f]$  is known, i.e.,

$$f(\vec{x}_{n+1}, t_{n+1}) \approx f(\vec{x}_n, t_n) + \Gamma[f] \Delta t, \quad (3)$$

where we use the compact notation  $\vec{x}_{n+1} := \vec{x}(t_{n+1}) = \vec{x}(t_n) + \vec{u} \Delta t$ .

In its most general form, the collision operator  $\Gamma[f]$  is a complex multi-dimensional integral that cannot be solved analytically and poses challenges even for those approaches that attempt to solve it numerically. The Bhatnagar-Gross-Krook (BGK) collision operator represents the simplest approximation that guarantees the conservation of mass and momentum and is given by ([Bhatnagar et al. 1954](#))

$$\Gamma[f] \approx -\frac{f - f^{\text{eq}}}{\tau}, \quad (4)$$

where  $\tau$  is the ‘‘relaxation time’’. In particular, it forces the particle distribution function  $f$  to decay to the local equilibrium  $f^{\text{eq}}$  at an exponential rate of  $e^{-t/\tau}$ ; for a classical non-relativistic fluid,  $f^{\text{eq}}$  is given by the Maxwell equilibrium distribution

$$f^{\text{eq}}(\rho, \vec{v}, \kappa, \vec{u}) = \frac{\rho}{(2\pi\kappa)^{D/2}} \exp\left[-\frac{(\vec{u} - \vec{v})^2}{2\kappa}\right], \quad (5)$$

where  $T, m$  are the local temperature and the mass of the one-component fluid,  $\vec{v}$  the local fluid velocity (first moment), and  $\kappa := k_B T/m$ .

Within the Chapman-Enskog analysis ([Chapman & Cowling 1970](#)), it is possible to show that the BGK collision operator is sufficient to restore the macroscopic properties of the fluid and, in particular, its dissipative properties, over a timescale that is related to the shear viscosity  $\nu = c_s^2(\tau - \Delta t/2)$ , where  $c_s$  is the fluid’s sound speed.

The key point of the LBM is the discretization of the underlying seven-dimensional phase space. More specifically, the  $N_{\text{dir}}$  discrete velocities  $\vec{u}_d$  are chosen such that the macroscopic first two moments can be computed exactly with a Hermite-Gauss quadrature

$$\rho(\vec{x}, t) = \int_{\mathbb{R}^D} f(\vec{x}, \vec{u}, t) d\vec{u} = \sum_{d=0}^{N_{\text{dir}}-1} f_d(\vec{x}, t), \quad (6)$$

$$\begin{aligned} \vec{v}(\vec{x}, t) &= \frac{1}{\rho(\vec{x}, t)} \int_{\mathbb{R}^D} f(\vec{x}, \vec{u}, t) \vec{u}(\vec{x}, t) d\vec{u} \\ &= \frac{1}{\rho(\vec{x}, t)} \sum_{d=0}^{N_{\text{dir}}-1} f_d(\vec{x}, t) \vec{u}_d(\vec{x}, t). \end{aligned} \quad (7)$$

This leads to a discretization of the distribution function

$$f_d(\vec{x}, t) = \frac{w_d}{\omega(\vec{u}_d)} f(\vec{x}, \vec{u}_d, t), \quad (8)$$

with weight function

$$\omega(\vec{u}_d) = \frac{1}{(2\pi)^{D/2}} e^{-\vec{u}_d^2/2}, \quad (9)$$

and quadrature weights  $w_d$ . Each population  $f_d$  accounts for the particles moving in the direction  $\vec{u}_d$ , and therefore, can be interpreted as a pseudo-particle.

Several different velocity stencils  $\{\vec{u}_d, w_d\}$ , with  $d = \{0, \dots, N_{\text{dir}} - 1\}$ , can be employed to guarantee the exact reconstruction of the macroscopic moments. Common choices are velocity stencils such that the velocities point from any source point to all neighbouring points on a Cartesian grid. In this way, no interpolation is needed and the LBM becomes a mass and momentum conservative scheme. The most commonly encountered stencils in two- (2D) and three-dimensions (3D) are the D2Q9 and D3Q27 stencils that we report in Fig. 1. The equilibrium distribution function is discretized similarly to the particle distribution function in a Hermite polynomial expansion,

$$f_d^{\text{eq}}(\rho, \vec{u}_d, \vec{v}) = w_d \rho \left[ 1 + \frac{\vec{u}_d \cdot \vec{v}}{c_s^2} + \frac{(\vec{u}_d \cdot \vec{v})^2}{2c_s^4} - \frac{\vec{v}^2}{2c_s^2} \right], \quad (10)$$

where a second-order expansion is sufficient since we need to integrate only the first three moments of the distribution (from zero to two).

The discretized form of Eq. (3) is given by

$$f_d(\vec{x}_{n+1}, t_{n+1}) = f_d(\vec{x}_n, t_n) + \Gamma_d(\vec{x}_n, t_n) \Delta t, \quad (11)$$

and can then be split into a two-step procedure

$$\text{Collision:} \quad f_d^* (\vec{x}_n, t_n) = f_d(\vec{x}_n, t_n) + \Gamma_d(\vec{x}_n, t_n) \Delta t, \quad (12)$$

$$\text{Streaming:} \quad f_d(\vec{x}_{n+1}, t_{n+1}) = f_d^* (\vec{x}_n, t_n). \quad (13)$$

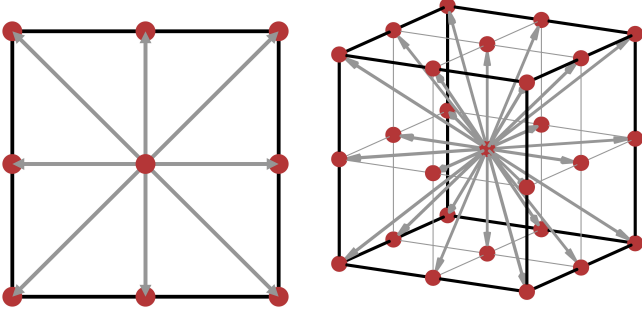


**Figure 1.** Discretisation stencils in 2D (left panel) and 3D (right panel). Red dots represent grid-points of the spatial discretization, while the grey arrows indicate the directions of the stencil. Besides the visible directions, the zero vector, pointing at the center, is also included in both velocity stencils.

The first step is the so-called ‘‘collision step’’ and accounts for the relaxation of the distribution function to the local equilibrium; it is purely local, meaning it only depends on quantities at a single lattice point. The second step is the so-called ‘‘streaming step’’, which simply moves populations of particles from one lattice point to its neighbours, according to the chosen velocity stencil. While the classical BGK collision operator conserves the moments, more complicated operators, e.g., those accounting for external forces, may not. Due to the nature of the collision process, the post-collision intensities are closer to the equilibrium state and produce more accurate moment integrals. Therefore, when using the moments for other operations, like coupling to other codes, it is important to use the moments computed directly after the collision step.

In summary, the lattice-Boltzmann method amounts to computing Eq. (12) for the collision step and Eq. (13) for the streaming step. When combined, these represent a system of  $N_{\text{dir}}$  coupled ODEs, where the coupling is hidden in the moments  $\rho$  and  $\vec{v}$  (see also [Succi 2001](#); [Krüger et al. 2017](#)) for additional details.

## 2.2 3+1 Split

A convenient way to handle the four-dimensional nature of spacetime as a manifold in general relativity is to decompose it into timelike and spacelike components by foliating it in terms of non-intersecting spacelike hypersurfaces  $\Sigma_t$  of constant coordinate time  $x^0 = t$  (see, e.g., [Misner et al. 1973](#); [Rezzolla & Zanotti 2013](#), for additional details). As customary, we define the ‘‘Eulerian’’ observer to be moving along a worldline orthogonal to  $\Sigma_t$  and thus tangent to the null-normalized local normal vector of  $\Sigma_t$

$$n_\mu = -\alpha \nabla_\mu t = (-\alpha, \vec{0}), \quad n^\mu = \frac{1}{\alpha} (1, -\beta^k), \quad (14)$$

where the lapse function  $\alpha$  can be seen as the time dilation of the Eulerian observer relative to a static observer at infinity, while the shift vector  $\beta^\mu$  is purely spatial and describes the coordinate changes intrinsic to the curvature of the spacetime. The metric associated with each hypersurface  $\Sigma_t$  is given by the spatial metric,

$$\gamma_{\mu\nu} = g_{\mu\nu} + n_\mu n_\nu, \quad \gamma^{\mu\nu} = g^{\mu\nu} + n^\mu n^\nu. \quad (15)$$

The unit normal  $n^\mu$  to a spacelike hypersurface  $\Sigma_t$  does not represent the direction along which the evolution needs to be carried out to obtain coordinate synchronous events on a new spacelike hypersurface. This is ensured by using the rescaled timelike vector

$$t^\mu = e_t^\mu = \alpha n^\mu + \beta^\mu. \quad (16)$$

Within this 3+1 split of spacetime, the four-metric can be expressed generally as

$$g_{\mu\nu} = \begin{pmatrix} -\alpha^2 + \beta_k \beta^k & \beta_j \\ \beta_i & \gamma_{ij} \end{pmatrix}, \quad (17)$$

$$g^{\mu\nu} = \begin{pmatrix} -1/\alpha^2 & \beta^j/\alpha^2 \\ \beta^i/\alpha^2 & \gamma^{ij} - \beta^i \beta^j/\alpha^2 \end{pmatrix}, \quad (18)$$

while an explicit expression for the extrinsic curvature  $K_{ij}$  in terms of the three-metric is given by

$$K_{ij} = \frac{1}{2\alpha} (2\gamma_{ik} \partial_j \beta^k + \partial_k \gamma_{ij} \beta^k - \partial_t \gamma_{ij}). \quad (19)$$

Additional relations that are useful when implementing the GRLBM are given by the derivatives of the four-metric and its components, and can be summarised as follows

$$\partial_\mu \alpha = \frac{\partial_\mu g^{00}}{2(-g^{00})^{3/2}}, \quad (20)$$

$$\partial_\mu \beta_i = \partial_\mu g_{0i}, \quad (21)$$

$$\partial_\mu \beta^i = \alpha^2 \partial_\mu g^{0i} + 2\alpha g^{0i} \partial_\mu \alpha, \quad (22)$$

$$\partial_\mu \gamma_{ij} = \partial_\mu g_{ij}, \quad (23)$$

$$\partial_\mu \gamma^{ij} = \partial_\mu g^{ij} + \frac{1}{\alpha^2} (\beta^i \partial_\mu \beta^j + \beta^j \partial_\mu \beta^i) - \frac{2}{\alpha^3} \beta^i \beta^j \partial_\mu \alpha. \quad (24)$$

## 2.3 Geodesic Equation

Let  $\tau$  be the proper time of the Eulerian observer and  $\lambda$  be an affine parameter along the photon null geodesic. The photon frequency measured by the Eulerian observer is then defined as,

$$v := \frac{d\tau}{d\lambda}, \quad (25)$$

so that we can decompose the photon four-momentum in terms of the four-velocity of the observer  $n^\mu$  and the photon four-velocity this observer measures  $v^\mu$ ,

$$p^\mu = \frac{dx^\mu}{d\lambda} = \frac{d\tau}{d\lambda} \frac{dt}{d\tau} \frac{dx^\mu}{dt} = v \frac{1}{\alpha} \kappa^\mu = v(n^\mu + v^\mu), \quad (26)$$

where  $dt/d\tau = n^0 = 1/\alpha$  and  $\kappa^\mu := dx^\mu/dt$  is the tangent to the photon worldline. The latter is related to the four-velocity of the Eulerian observer and the three-velocity of the photon as observed by such an observer by the relations

$$\frac{dx^\mu}{dt} = \kappa^\mu = \alpha (n^\mu + v^\mu), \quad (27)$$

$$\frac{dx^0}{dt} = \kappa^0 = 1 = \alpha \left( \frac{1}{\alpha} + v^0 \right) \Rightarrow v^0 = 0, \quad (28)$$

$$\frac{dx^i}{dt} = \kappa^i = \alpha (n^i + v^i) = \alpha \left( -\frac{\beta^i}{\alpha} + v^i \right) = \alpha v^i - \beta^i, \quad (29)$$

where the normalisation of these four-vectors are

$$\kappa_\mu \kappa^\mu = 0, \quad n_\mu n^\mu = -1, \quad v_\mu v^\mu = v_i v^i = 1. \quad (30)$$

The coordinate-time dependent geodesic equations can then be written in 3+1-form as ([Vincent et al. 2012](#))

$$\frac{dv}{dt} = v(\alpha K_{ij} v^i v^j - v^i \partial_i \alpha), \quad (31)$$

$$\frac{dx^i}{dt} = \alpha v^i - \beta^i, \quad (32)$$

$$\frac{dv^i}{dt} = \alpha v^j \left[ v^i (\partial_j \ln \alpha - K_{jk} v^k) + 2K^i_j - {}^3\Gamma^i_{jk} v^k \right] - \gamma^{ij} \partial_j \alpha - v^j \partial_j \beta^i. \quad (33)$$

### 3 SPECIAL-RELATIVISTIC LATTICE-BOLTZMANN METHOD FOR RADIATIVE TRANSPORT

An obvious starting point to introduce our GRLBM is to briefly summarise the special-relativistic approach proposed by [Weih et al. \(2020c\)](#), where it is necessary to differentiate between the laboratory frame (LF) and the fluid frame (FF), which we indicate using tilded variables.

Let  $\mathcal{P}$  be a photon bundle at the spacetime position  $x^\mu$ , three-velocity  $v^i$ , and four-momentum  $p^\mu$ . The evolution of its Lorentz-invariant distribution function,  $f_\nu = f(x^i, v^i, \nu, t) = \tilde{f}_{\tilde{\nu}}$ , is then governed by the radiative Boltzmann equation

$$\frac{df_\nu}{d\lambda} = \frac{\eta_\nu}{\nu^2} - \nu \kappa_{a\nu} f_\nu + \Gamma_\nu[f_\nu] =: C_\nu[f_\nu], \quad (34)$$

where  $\nu := p^0 = dt/d\lambda$  is the frequency observed in the laboratory frame,  $\eta_\nu$  the fluid emissivity,  $\kappa_{a\nu}$  the fluid absorption coefficient,  $\Gamma_\nu$  the scattering operator, and  $C_\nu$  the total collision operator. The explicit form of the scattering operator  $\Gamma_\nu[f_\nu]$  depends on the underlying scattering model. Following [Weih et al. \(2020c\)](#), we assume a homogeneous iso-energetic scattering operator, which is simpler to express in the comoving FF (see Appendix B for full derivation) as

$$\tilde{\Gamma}_{\tilde{\nu}}[\tilde{f}_{\tilde{\nu}}] = \tilde{\nu} [\tilde{\kappa}_{0\tilde{\nu}}(\tilde{E}_{\tilde{\nu}} - \tilde{f}_{\tilde{\nu}}) + 3\tilde{\kappa}_{1\tilde{\nu}}\tilde{\nu}_i\tilde{F}_{\tilde{\nu}}^i], \quad (35)$$

where  $\tilde{\kappa}_{0\tilde{\nu}}$  and  $\tilde{\kappa}_{1\tilde{\nu}}$  are the zeroth and first-order scattering coefficients in the FF of an underlying Legendre expansion (see Appendix B for more detail), accounting for the isotropic and forward scattering, respectively.

Because in the FF we know both the explicit form of the scattering operator, and obviously the fluid properties  $\tilde{\eta}_{\tilde{\nu}}$ ,  $\tilde{\kappa}_{a\tilde{\nu}}$ ,  $\tilde{\kappa}_{0\tilde{\nu}}$ ,  $\tilde{\kappa}_{1\tilde{\nu}}$ , we can express the Boltzmann equation (34) in the FF as

$$\frac{d\tilde{f}_{\tilde{\nu}}}{d\lambda} = \frac{\tilde{\eta}_{\tilde{\nu}}}{\tilde{\nu}^2} - \tilde{\nu}\tilde{\kappa}_{a\tilde{\nu}}\tilde{f}_{\tilde{\nu}} + \tilde{\nu} \left( \tilde{\kappa}_{0\tilde{\nu}}(\tilde{E}_{\tilde{\nu}} - \tilde{f}_{\tilde{\nu}}) + 3\tilde{\kappa}_{1\tilde{\nu}}\tilde{\nu}_i\tilde{F}_{\tilde{\nu}}^i \right). \quad (36)$$

Next, we transform the affine parameter differential to the LF time differential by using the chain rule and replace the distribution function  $\tilde{f}_{\tilde{\nu}}$  with the specific intensity  $\tilde{I}_{\tilde{\nu}} = \tilde{\nu}^3 \tilde{f}_{\tilde{\nu}}$ . The Lorentz transformation of the frequency can be derived by boosting the photon four-momentum  $p^\mu$  between inertial frames (see Appendix A)

$$\frac{d\tilde{f}_{\tilde{\nu}}}{d\lambda} = \frac{dt}{d\lambda} \frac{d\tilde{f}_{\tilde{\nu}}}{dt} = \nu \frac{d\tilde{f}_{\tilde{\nu}}}{dt} = \frac{\tilde{\nu}}{A} \frac{d(\tilde{I}_{\tilde{\nu}}/\tilde{\nu}^3)}{dt}, \quad (37)$$

so that

$$\frac{d\tilde{I}_{\tilde{\nu}}}{dt} = A\tilde{\nu}^2 \frac{d\tilde{f}_{\tilde{\nu}}}{d\lambda} = A\tilde{\nu}^2 \tilde{C}_{\tilde{\nu}}[\tilde{f}_{\tilde{\nu}}] \quad (38)$$

$$= A \left[ \tilde{\eta}_{\tilde{\nu}} - \tilde{\kappa}_{a\tilde{\nu}}\tilde{I}_{\tilde{\nu}} + \tilde{\kappa}_{0\tilde{\nu}}(\tilde{\nu}^3 \tilde{E}_{\tilde{\nu}} - \tilde{I}_{\tilde{\nu}}) + 3\tilde{\kappa}_{1\tilde{\nu}}\tilde{\nu}_i\tilde{\nu}^3 \tilde{F}_{\tilde{\nu}}^i \right], \quad (39)$$

and where

$$A := \gamma(1 - u_i v^i) = \frac{1 - u_i v^i}{\sqrt{1 - u_i u^i}}, \quad (40)$$

is the Doppler factor between the LF and FF, and  $u^i$  the three-velocity of the fluid measured in the LF.

Since we are not interested in the monochromatic intensity  $I_\nu$ , but rather in the total or ‘‘grey’’ (or frequency-integrated) intensity  $I$ , we

also define the total emissivity, opacities, and moments

$$I := \int_0^\infty I_\nu d\nu, \quad (41)$$

$$\eta := \int_0^\infty \eta_\nu d\nu, \quad (42)$$

$$\kappa_{\star} := \frac{\int_0^\infty \kappa_{\star\nu} I_\nu d\nu}{\int_0^\infty I_\nu d\nu}, \quad \star \in \{a, 0, 1\} \quad (43)$$

$$E := \int_0^\infty \nu^3 E_\nu d\nu = \frac{1}{4\pi} \oint_{4\pi} \int_0^\infty \nu^3 f_\nu d\nu d\Omega = \frac{1}{4\pi} \oint_{4\pi} I d\Omega, \quad (44)$$

$$F^i := \int_0^\infty \nu^3 F_\nu^i d\nu = \frac{1}{4\pi} \oint_{4\pi} \int_0^\infty \nu^3 f_\nu v^i d\nu d\Omega = \frac{1}{4\pi} \oint_{4\pi} I v^i d\Omega. \quad (45)$$

Applying this ‘grey’ approximation to Eq. (38), we get,

$$\frac{d\tilde{I}}{dt} = A [\tilde{\eta} - (\tilde{\kappa}_a + \tilde{\kappa}_0)\tilde{I} + \tilde{\kappa}_0\tilde{E} + 3\tilde{\kappa}_1\tilde{\nu}_i\tilde{F}^i] \quad (46)$$

$$= A [\tilde{\eta} - (\tilde{\kappa}_a + \tilde{\kappa}_0)\tilde{I} + \tilde{M}], \quad (47)$$

where we introduced the moment collision term

$$\tilde{M} := \tilde{\kappa}_0\tilde{E} + 3\tilde{\kappa}_1\tilde{\nu}_i\tilde{F}^i, \quad (48)$$

in terms of the zero and first-order scattering coefficients  $\kappa_0$  and  $\kappa_1$ . The next step is to transform the total intensities from the FF to the LF by applying the respective Lorentz transformation law, see Eq. (A18). The mixed frame ODE for the total LF intensity can then be expressed as,

$$\frac{dI}{dt} = \frac{\tilde{\eta} + \tilde{M}}{A^3} - AI(\tilde{\kappa}_a + \tilde{\kappa}_0), \quad (49)$$

which is the same as Eq. (B8) in [Weih et al. \(2020c\)](#). Specialisations to a one-dimensional (two-dimensional) case is obtained with the following change  $A^3 \rightarrow A$  ( $A^3 \rightarrow A^2$ ) in Eq. (49).

#### 3.1 Numerical discretization

When seeking a numerical solution we obviously need to discretize the total intensity  $I$  into the  $N_{\text{dir}}$  population intensities  $I_d$ ,

$$I_d(x^i, t) := I(x^i, v_d^i, t), \quad (50)$$

$$\frac{dI_d}{dt} = \frac{\tilde{\eta} + \tilde{M}_d}{A_d^3} - A_d I_d(\tilde{\kappa}_a + \tilde{\kappa}_0), \quad (51)$$

where, unlike the classical LBM, we did not include the weights in the definition of the population intensities; a similar approach will be necessary for the GRLBM, as we will see in Sec. 4.

As a result, the weights  $w_d$  of the numerical quadratures must be included when calculating the moments

$$E = \frac{1}{4\pi} \oint_{4\pi} I d\Omega \approx \sum_{d=0}^{N_{\text{dir}}-1} w_d I_d, \quad (52)$$

$$F^i = \frac{1}{4\pi} \oint_{4\pi} v^i I d\Omega \approx \sum_{d=0}^{N_{\text{dir}}-1} w_d I_d v_d^i, \quad (53)$$

$$P^{ij} = \frac{1}{4\pi} \oint_{4\pi} v^i v^j I d\Omega \approx \sum_{d=0}^{N_{\text{dir}}-1} w_d I_d v_d^i v_d^j. \quad (54)$$

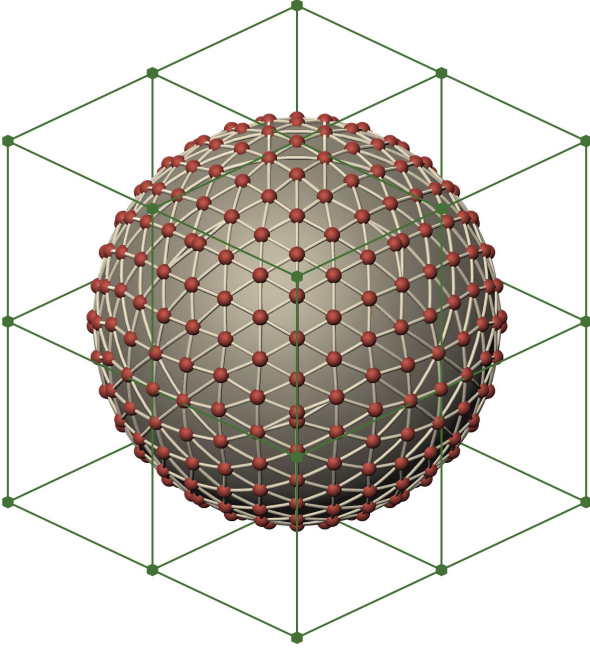


**Figure 2.** Lebedev stencil of order  $p_{\text{Leb}} = 31$  with 351 discrete points (red dots) for the quadrature of the velocities on the two-sphere.

Note that the set of discretized velocities  $v_d^i$  is restricted to lie on the unit sphere due to the absolute speed of photons, so that the Hermite-Gauss quadrature is not applicable anymore. Instead, we use spherical quadratures in 2D and 3D, which aim to integrate Fourier- and spherical-harmonics as well as possible. The number of directions in our velocity stencil must be much higher than in the classical LBM to ensure that the moments are integrated to an acceptable degree of accuracy. Furthermore, besides the accuracy of the moment integrations, a large number of populations is also essential for the free-streaming scenario in optically-thin media, where a large number of homogeneously distributed points must be used to achieve homogeneous propagation of light beams.

As a result, we use a Fourier quadrature with homogeneous velocity distribution in 2D and a Lebedev quadrature of order  $p_{\text{Leb}}$  in 3D as shown in Fig. 2 for a unit two-sphere, which is a 2D surface in a 3D space. Our tests have shown that in 2D, at least 50 directions and in 3D, at least 200 directions are needed for homogeneous propagation. Generally speaking, more directions are always better, but no significant improvement can be seen in 2D beyond 200. This said, and as we will comment further in Sec. 4.2.2, to reduce computational costs, the stencils can also be suitably modified so as to use fewer directions while achieving the desired accuracy.

Generally speaking, Eqs. (50) and (51) represent a stiff system of  $N_{\text{dir}}$  coupled ODEs. The stiffness stems from the wide range of possible emissivity and opacity values and mostly appears in optically-thick regimes. Therefore, a forward Euler scheme will not be stable for all possible values of  $\tilde{\eta}$ ,  $\tilde{\kappa}_a$ ,  $\tilde{\kappa}_0$ ,  $\tilde{\kappa}_1$ . Instead, we must employ an implicit integrator like the backward Euler method. However, solving an  $N_{\text{dir}} \times N_{\text{dir}}$  linear system every timestep on every grid-point is not feasible given high number of populations we need to use. A quicker alternative is the so-called ‘‘Lambda-iteration’’ scheme, that is, a fixed-point iteration method that converges to the solution of the linear system (Hubeny 2003).

By expressing our system of ODEs in matrix form

$$\frac{d\vec{I}}{dt} = \Lambda \vec{I}, \quad (55)$$

we can split the matrix  $\Lambda$  into two parts

$$\Lambda = \Phi + (\Lambda - \Phi) = \Phi + \Psi, \quad (56)$$

where  $\Phi$  should be easily invertible, e.g., diagonal. Applying the implicit Euler integrator, we can rearrange the system of ODEs to obtain an expression for the new timestep at level  $n$

$$\vec{I}_n = \vec{I}_{n-1} + \Delta t [\Phi + \Psi] \vec{I}_n, \quad (57)$$

so that

$$\vec{I}_n = [1 - \Delta t \Phi]^{-1} [\vec{I}_{n-1} + \Delta t \Psi \vec{I}_n]. \quad (58)$$

Since  $\vec{I}_n$  appears also on the right-hand side of Eq. (58), this expression is not explicit. However, if we replace  $\vec{I}_n$  with a guess for it,  $\vec{I}_n^{(0)}$ , e.g., the value from the previous  $n - 1$  timestep  $\vec{I}_n^{(0)} = \vec{I}_{n-1}$ , the equation above becomes an estimate for  $\vec{I}_n$ . Repeating this process with the new estimate, we get an iterative scheme

$$\vec{I}_n^{(m+1)} = [1 - \Delta t \Phi]^{-1} [\vec{I}_{n-1} + \Delta t \Psi \vec{I}_n^{(m)}], \quad (59)$$

that converges to the solution of the initial system of ODEs,

$$\vec{I}_n = \lim_{m \rightarrow \infty} \vec{I}_n^{(m)}. \quad (60)$$

In the case of Eq. (51), the linear terms are given by  $A_d J_d (\tilde{\kappa}_a + \tilde{\kappa}_0)$ , and the components in the FF moments,  $\tilde{E}$  and  $\tilde{F}^i$ , that are proportional to  $I_d$ . Disentangling the linear terms from the FF moments is algebraically and computationally very difficult and not necessary to achieve good results with the Lambda-iteration method. Instead, we only use the expression  $A_d J_d (\tilde{\kappa}_a + \tilde{\kappa}_0)$  for the operator split and apply the Lambda-iteration to our system of ODEs in Eq. (50) and in Eq. (51) to get

$$I_d^{(m+1)}(x_n^i, t_n) = \frac{I_d^{(0)}(x_{n-1}^i, t_{n-1}) + \Delta t (\tilde{\eta} + \tilde{M}_d^{(m)}) / A_d^3}{1 + \Delta t A_d (\tilde{\kappa}_a + \tilde{\kappa}_0)}, \quad (61)$$

where

$$\tilde{M}_d^{(m)} := \tilde{\kappa}_0 \tilde{E}^{(m)} + 3\tilde{\kappa}_1 \tilde{v}_{d,i} \tilde{F}^i{}^{(m)}, \quad (62)$$

and with an upper limit on the number of iterations set to  $m \leq 100$ .

As in the classical LBM case, before we start iterating Eq. (61), we split it into two steps<sup>1</sup>

$$I_d^{\star(m+1)}(y^i, t_{n-1}) = \frac{I_d^{(0)}(y^i, t_{n-1}) + \Delta t (\tilde{\eta} + \tilde{M}_d^{(m)}) / A_d^3}{1 + \Delta t A_d (\tilde{\kappa}_a + \tilde{\kappa}_0)}, \quad (63)$$

and

$$I_d(x_n^i, t_n) = I_d^{\star(\text{final})}(x_{n-1}^i, t_{n-1}), \quad (64)$$

where Eq. (63) is the collision step, which now consists of the Lambda-iteration scheme, locally at a grid-point  $y^i$ . This equation should be iterated until all the post-collision intensities  $I_d^{\star}$  converge. In practice, we iterate until the first three moments  $E$ ,  $F^i$ ,  $P^{ij}$  converge to a desired precision.

In the second step, i.e., in the streaming step (64), the velocities  $v_d^i$  of the spherical stencils do not reach the neighbouring grid-points

<sup>1</sup> We recall that the  $\star$  is commonly used throughout the literature in the LBM for the post-collision populations  $f_d^{\star}$ , to distinguish them from the usual populations  $f_d$ .

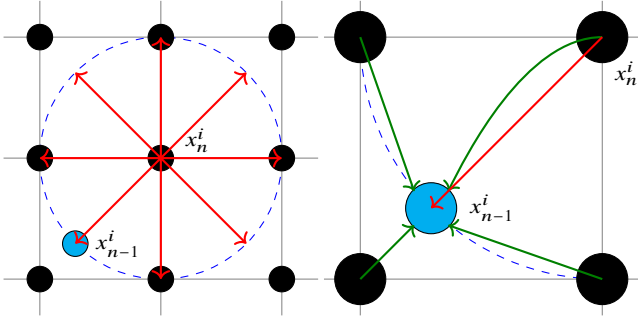


**Figure 3.** Radiation streaming with spatial interpolation. *Left panel:* Velocity vectors (red) do not reach the nearest neighbouring grid-points (black). *Right panel:* Post-collision intensities must be interpolated (green arrows) to the off-grid grid-point (light blue dot) and streamed to the target grid-point (red arrow).

(see left panel of Fig. 3). This requires a spatial interpolation of the post-collision intensities  $I_d^{\star(\text{final})}(y^i)$  to the off-grid grid-point  $x_{n-1}^i$ . The streaming step then carries the interpolated post-collision intensity from the off-grid source point  $x_{n-1}^i$  to the target point  $x_n^i$  (see right panel of Fig. 3). While our tests have shown that a linear interpolation is sufficient in this step, it also introduces numerical dispersion and breaks to a small extent the perfectly conservative nature of the SRLBM.

Defining the relative mean-square error of the moments of as

$$\epsilon := \left( \frac{\bar{E}_n - \bar{E}_{n-1}}{\bar{E}_n} \right)^2 + \sum_i \left( \frac{\bar{F}_n^i - \bar{F}_{n-1}^i}{\bar{F}_n^i} \right)^2 + \sum_{i,j} \left( \frac{\bar{P}_n^{ij} - \bar{P}_{n-1}^{ij}}{\bar{P}_n^{ij}} \right)^2. \quad (65)$$

We have tested the convergence rate of the Lambda-iteration scheme in an optically thick regime with  $\tilde{\kappa}_0 = 10^5$  with a threshold of  $\epsilon < 10^{-10}$ . While the average iteration count remains at roughly 4, the maximum iteration count reaches the limit of  $m = 100$  at the beginning of some simulations, suggesting that the initial intensity distribution is not in equilibrium. This behavior is to be expected, as we have no control over the initial pressure density (see Appendix D), which is needed for adequate initial data. Overall, our finding is that the first few timesteps allow the radiation to equalise, drastically decreasing the needed iteration count for the Lambda-iteration scheme.

### 3.2 Coupling to background matter

So far, we have only discussed how the radiation field is influenced by the background matter fluid. Of course, we are equally interested in the back-reaction that the radiation has on the fluid properties, that is, energy and momentum. These contributions can be incorporated using the following logical procedure.

(i) For every timestep, compute the fluid frame emissivity  $\tilde{\eta}$  and opacity coefficients  $\tilde{\kappa}_{a/0/1}$ , from the fluid rest-mass density  $\rho$ , temperature  $T$ , and three-velocity  $u^i$ .

(ii) As the conservative MHD variables are evolved in time, the  $N_{\text{dir}}$  populations of the radiation intensities,  $I_d$  are also evolved and the LF moments computed via the collision and streaming steps.

(iii) The LBM transforms the newly computed LF moments into the FF.

(iv) From the FF moments, the radiative source terms  $S_0$  and  $S_k$

given by Eqs. (66)–(69) are computed as follows

$$S_0 = \gamma(\tilde{\kappa}_a \tilde{E} - \tilde{\eta}) + \tilde{\kappa} H_0, \quad (66)$$

$$S_i = \gamma(\tilde{\kappa}_a \tilde{E} - \tilde{\eta}) u_i + \tilde{\kappa} H_i, \quad (67)$$

where

$$\tilde{\kappa} = \tilde{\kappa}_a + \tilde{\kappa}_s = \tilde{\kappa}_a + (\tilde{\kappa}_0 - \tilde{\kappa}_1/3), \quad (68)$$

$$H_i = \gamma^3 (F^m u_m - E) u_i + \gamma h_{im} F^m - \gamma h_{il} u_m P^{lm}. \quad (69)$$

These quantities are then used for the subsequent MHD evolution.

## 4 GENERAL-RELATIVISTIC LATTICE-BOLTZMANN METHOD FOR RADIATIVE TRANSPORT

### 4.1 Mathematical Strategy

Within a general-relativistic formulation of the lattice-Boltzmann equations for radiative transport, it is necessary to differentiate among three frames: the Lab Frame (LF; for which we do not use any special notation), the Eulerian (or inertial) frame (EF, for which we use barred variables), and the Fluid Frame (FF; for which we employ tilded variables). Transformations among all these frames need to be made using Lorentz transformations.

Given the equivalence among these three frames, a decision should be taken on the optimal frame where to express the evolution equation of the total intensity. Inevitably, this decision also affects the frame in which we discretize the velocity space. Because we want to preserve the quadratures we employ in the SRLBM, the LF would not represent a useful choice. Indeed, if we were to discretize the four-velocities  $v^\mu$  in the LF, neither the spatial components  $v^k$ , nor the three-velocity as seen by the Eulerian observer  $\tilde{v}^k$  trace a spherical shape, breaking the spherical quadrature. In addition, when deriving quadrature rule in the LF we would need to choose weights that differ for every grid-point and change over time in a dynamical spacetime (only a local inertial frame preserves the isotropy in the quadrature weights). On the other hand, using the FF introduces additional Lorentz-boosts when comparing velocities, as the fluid velocity may vary substantially between neighbouring grid-points. Finally, within the EF we can assume that the four-velocities of neighbouring observers are similar enough, allowing us direct comparison between directions without a Lorentz-boosting. Doing so also implies that the local neighbourhood is flat enough to ignore additional effects from parallel transport of vectors between neighbouring grid-points. In view of these considerations, we have concluded the EF to be the most convenient to discretize the velocities and in the following we derive the total intensity evolution equation only for the EF.

We start by expressing the Boltzmann equation in the FF and transform the affine derivative into the LF time derivative via the chain rule,

$$\frac{d\tilde{f}_{\tilde{v}}}{d\lambda} = \frac{dt}{d\lambda} \frac{d\tilde{f}_{\tilde{v}}}{dt} = \frac{v}{\alpha} \frac{d\tilde{f}_{\tilde{v}}}{dt} = \frac{\tilde{v}}{\alpha A} \frac{d(\tilde{I}_{\tilde{v}}/\tilde{v}^3)}{dt}, \quad (70)$$

so that

$$\frac{d(\tilde{I}_{\tilde{v}}/\tilde{v}^3)}{dt} = \frac{\alpha A}{\tilde{v}} \frac{d\tilde{f}_{\tilde{v}}}{d\lambda} = \frac{\alpha A}{\tilde{v}} \tilde{C}_{\tilde{v}}[\tilde{f}_{\tilde{v}}], \quad (71)$$

and where we can use the same FF collision operator  $\tilde{C}_{\tilde{v}}[\tilde{f}_{\tilde{v}}]$  employed in Eq. (38).

Unlike the SRLBM, the LF is not a Lorentz frame, thus gaining additional  $\alpha$  (lapse) in the denominator, stemming from the time dilation between the EF and the LF. In addition, the frequency  $\tilde{v}$  is not constant along the photon path due to gravitational redshift, so

that we cannot separate the frequency from the intensity as we did in Eq. (38). As a result, we need to perform the time integration before we can use the grey approximation

$$\int_{t_{n-1}}^{t_n} \frac{d(\tilde{I}_{\tilde{\nu}}/\tilde{\nu}^3)}{dt} dt = \frac{\tilde{I}_{\tilde{\nu}_n}}{\tilde{\nu}_n^3} - \frac{\tilde{I}_{\tilde{\nu}_{n-1}}}{\tilde{\nu}_{n-1}^3} = \int_{t_{n-1}}^{t_n} \alpha A \frac{\tilde{C}_{\tilde{\nu}}[\tilde{f}_{\tilde{\nu}}]}{\tilde{\nu}} dt, \quad (72)$$

where we have introduced the short-hand notation  $\tilde{I}_{\tilde{\nu}_n} := \tilde{I}_{\tilde{\nu}(t_n)}(x^i(t_n), \tilde{\nu}^i(t_n), t_n)$ .

For the right-hand side of Eq. (72), we use a forward Euler integration and assume that the lapse and the fluid properties are approximately constant to prevent strong coupling between the GRMHD and radiation solvers. As a result,  $\alpha = \alpha_{n-1} \approx \alpha_n$ ,  $\tilde{\eta}_{\tilde{\nu}} = \tilde{\eta}_{\tilde{\nu}_{n-1}} \approx \tilde{\eta}_{\tilde{\nu}_n}$ , and,  $\tilde{\kappa}_{\star\tilde{\nu}} = \tilde{\kappa}_{\star\tilde{\nu}_{n-1}} \approx \tilde{\kappa}_{\star\tilde{\nu}_n}$ , for  $\star \in \{a, 0, 1\}$ . Under these assumptions, we can write

$$\tilde{I}_{\tilde{\nu}_n} = \tilde{s}^3 \tilde{I}_{\tilde{\nu}_{n-1}} + \alpha \Delta t A_n \left[ \tilde{\eta}_{\tilde{\nu}_n} - \tilde{\kappa}_a \tilde{\nu}_n \tilde{I}_{\tilde{\nu}_n} + \tilde{\kappa}_0 \tilde{\nu}_n (\tilde{\nu}_n^3 \tilde{E}_{\tilde{\nu}_n} - \tilde{I}_{\tilde{\nu}_n}) + 3\tilde{\kappa}_1 \tilde{\nu}_n \tilde{\nu}_n^3 \tilde{\nu}_{n,i} \tilde{F}_{\tilde{\nu}_n}^i \right], \quad (73)$$

so that the new variable  $\tilde{s}$  measuring the ratio of the received and emitted frequencies can be considered the ‘‘redshift factor’’ which assumes different values in different frames, namely

$$s = \frac{\nu_n}{\nu_{n-1}} \approx \frac{1}{1 - \Delta t (\alpha K_{ij} \nu^i \nu^j - \nu^i \partial_i \alpha)}, \quad (\text{LF}), \quad (74)$$

$$\tilde{s} = \frac{\tilde{\nu}_n}{\tilde{\nu}_{n-1}} = \frac{\alpha_n \nu_n}{\alpha_{n-1} \nu_{n-1}} \approx \frac{\nu_n}{\nu_{n-1}} = s, \quad (\text{EF}), \quad (75)$$

$$\tilde{s} = \frac{\tilde{\nu}_n}{\tilde{\nu}_{n-1}} = \frac{\nu_n}{\nu_{n-1}} \frac{A_n}{A_{n-1}} = \tilde{s} \frac{A_n}{A_{n-1}} = s \frac{A_n}{A_{n-1}}, \quad (\text{FF}). \quad (76)$$

Note that because the redshift factor is the same at all frequencies, we take it out of the frequency integral in the grey approximation  $\int_0^\infty \dots d\tilde{\nu}_n$  and obtain

$$\tilde{I}_n = \tilde{s}^4 \tilde{I}_{n-1} + \alpha \Delta t A_n \left[ \tilde{\eta} - (\tilde{\kappa}_a + \tilde{\kappa}_0) \tilde{I}_n + \tilde{M}_n \right], \quad (77)$$

$$\tilde{M}_n = \tilde{\kappa}_0 \tilde{E}_n + 3\tilde{\kappa}_1 \tilde{\nu}_{n,i} \tilde{F}_n^i. \quad (78)$$

As in the SRLBM, we can employ here the Lambda-Iteration scheme for the evolution equation for the total intensity in the FF

$$\tilde{I}_n^{(m+1)} = \frac{\tilde{s}^4 \tilde{I}_{n-1} + \alpha \Delta t A_n (\tilde{\eta} + \tilde{M}^{(m)})}{1 + \alpha \Delta t A_n (\tilde{\kappa}_a + \tilde{\kappa}_0)}, \quad (79)$$

$$\tilde{M}^{(m)} = \tilde{\kappa}_0 \tilde{E}_n^{(m)} + 3\tilde{\kappa}_1 \tilde{\nu}_{n,i} \tilde{F}_n^{i(m)}, \quad (80)$$

where  $\tilde{I}_n^{(0)} = \tilde{I}_{n-1}$ . On the other hand, for the evolution equation in the EF, we have to transform the total intensities  $\tilde{I}_n = \tilde{I}_n A_n^4$  and the redshift factor  $\tilde{s} = s A_n / A_{n-1}$  to obtain

$$\tilde{I}_n^{(m+1)} = \frac{s^4 \tilde{I}_{n-1} + \alpha \Delta t \left( \tilde{\eta} + \tilde{M}^{(m)} \right) / A_n^3}{1 + \alpha \Delta t A_n (\tilde{\kappa}_a + \tilde{\kappa}_0)}, \quad (81)$$

where, again,  $\tilde{I}_n^{(0)} = \tilde{I}_{n-1}$ . Next, we perform the velocity discretization

$$\tilde{I}_d(x^i, t) = s_d^4 \tilde{I}(x^i, \tilde{\nu}_d^i, t), \quad (82)$$

$$\tilde{I}_d^*(x^i, t) = \frac{\tilde{I}_d(x^i, t)}{s_d^4}, \quad (83)$$

and drop the timestep dependency on  $A_n$  and replace it with a direction dependency  $A_d$ . By absorbing the redshift factor into the discretized intensities, we can move the evaluation of the redshift

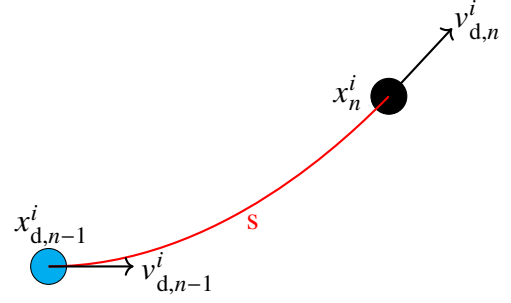


**Figure 4.** Curved radiation streaming of single direction. The origin of the radiation bundle (light blue dot)  $x_{d,n-1}^i$  is computed by following the geodesic path (red line) backwards in time from the target point (black dot)  $x_n^i$ . Note that the velocities at the start and end do not match.

factor to the streaming step.

$$\tilde{I}_d^{*(m+1)}(y^i, t_{n-1}) = \frac{\tilde{I}_d^{(0)}(y^i, t_{n-1}) + \alpha \Delta t \left( \tilde{\eta} + \tilde{M}_d^{(m)} \right) / A_d^3}{1 + \alpha \Delta t A_d (\tilde{\kappa}_a + \tilde{\kappa}_0)}, \quad (84)$$

$$\tilde{M}_d^{(m)} = \tilde{\kappa}_0 \tilde{E}^{(m)} + 3\tilde{\kappa}_1 \tilde{\nu}_{d,i} \tilde{F}^{i(m)}, \quad (85)$$

$$\tilde{I}_d(x_n^i, \tilde{\nu}_{d,n}^i, t_n) = s_d^4 \tilde{I}_d^{*(\text{final})}(x_{d,n-1}^i, \tilde{\nu}_{d,n-1}^i, t_{n-1}). \quad (86)$$

Doing so, removes all the additional complexity from the collision step (84) and transfers it to the streaming step (86).

Comparing our newly derived collision operation (84) to that of the SRLBM (63), we can see that they are identical except for the lapse  $\alpha$ . At first glance, the streaming step might seem very similar as well. However, in the special-relativistic scenario, the propagation direction of light remains constant, i.e.,  $\nu_n^i = \nu_{n-1}^i$ , allowing the  $N_{\text{dir}}$  discrete intensities to propagate independently from one another. In the general-relativistic case, however, the direction of propagation of light varies, i.e.,  $\tilde{\nu}_n^i \neq \tilde{\nu}_{n-1}^i$ , effectively introducing an interpolation step in the velocity space and thus a direct inter-dependency of the discretized intensities. For this reason, we did not include the weights in the definition of the discretized intensities in the previous section. Indeed, intensity interpolation in the velocity space would not be possible when including the weights in the definition.

Note also that the streaming step is more complex in a general-relativistic context (see Fig. 4). First, we must determine the off-grid source point  $x_{d,n-1}^i$  (light blue dot), the source velocity  $\tilde{\nu}_{d,n-1}^i$ , and the redshift factor  $s$  by integrating the geodesic equations (31)–(33) backward in time. The initial data is the target point  $x_n^i$  (black dot) and target direction  $\tilde{\nu}_{d,n}^i$ , and we solve the equations with a fourth order adaptive Runge-Kutta-Fehlberg integrator. We note that repeating doing this operation for  $N_{\text{dir}}$  populations is computationally expensive. In Sec. 4.2.2, we introduce an interpolation scheme to reduce the number of ODEs drastically.

Once the geodesic equations are solved, we would need to parallel transport the source  $\tilde{\nu}_{d,n-1}^i$  velocity to the neighbouring grid-points along some specified path. For simplicity, we assume that the spatial discretization is fine enough and that the local curvature does not vary significantly, so that the parallel transport can be replaced by a simple interpolation. The testing we will discuss in Sec. 5 shows that this is a very reasonable approximation, even in the vicinity of a black hole horizon. However, special care must be taken if the radiation field is composed mainly of photon bundles orbiting very close to the horizon.

Next, we perform velocity-space interpolation, for which we employ a quadratic scheme in 2D and, due to the unstructured nature of Lebedev stencils, a Voronoi interpolation scheme in 3D (Bobach

2009). As in the SRLBM, linear interpolation is sufficient for the spatial interpolation. However, due to the underlying curved spacetime, each grid point experiences a different time dilation which affects the measured intensities. Therefore, we transform all intensities from the neighbouring grid points (B) to the receiving observer (A) at  $x_n^i$  via a simple algebraic expression

$$I_A = \left( \frac{\alpha_A}{\alpha_B} \right)^4 I_B. \quad (87)$$

Finally, we are interested in the moments in the LF and to transform the moments from the EF to the LF, we apply a tetrad transformation to the relevant tensors. In particular, building the energy-momentum of the radiation field in the Eulerian frame as

$$\bar{T}^{\mu\nu} = \sum_d \begin{pmatrix} 1 & \bar{n}_d^j \\ \bar{n}_d^i & \bar{n}_d^i \bar{n}_d^j \end{pmatrix} w_d \bar{I}_d = \begin{pmatrix} \bar{E} & \bar{F}^j \\ \bar{F}^i & \bar{P}^{ij} \end{pmatrix}, \quad (88)$$

so that the energy-momentum of the radiation field in the LF will be given by (see Appendix C for the explicit expression of the tetrad)

$$T^{\mu\nu} = e^\mu_\alpha e^\nu_\beta \bar{T}^{\alpha\beta}. \quad (89)$$

Due to our definition of the discretized intensities, the moment quadrature would also need to change

$$\bar{E} = \sum_d \frac{w_d \bar{I}_d}{s_d^A} = \sum_d w_d \bar{I}_d^*. \quad (90)$$

We should note that the inclusion of the frequency shifts  $s_d$  in the quadrature computation is very costly and increases the computational time of factor of almost 15. In the tests carried out here and discussed below, we have evaluated the solution with and without the frequency shift in Eq. (90) finding only negligible differences.

As a result, our implementation of the GRLBM is such that in the Lambda-Iteration scheme the initial moments are computed with  $\bar{E} \approx \sum_d w_d \bar{I}_d$ , leading to a minor error in the initial moments. However, in all consecutive steps of the Lambda-Iteration, we compute the moments from the iterated intensities using the exact expression (90). Combined with the iteration scheme's convergence criteria, this leads to a self-correcting behavior, where any small mistakes in the initial moments are subsequently corrected. At the same time, we note that the frequency shift in the streaming step is essential for correctly propagating the intensities.

As a concluding remark, we note that when entering optically-thick regimes, the GRLBM is subject to the Courant-Friedrichs-Lewy (CFL) condition like any solver in the diffusive limit. While it is advisable to use the same CFL coefficient as that employed in the solution of the GRMHD equations, usually around 0.2, to ensure synchronisation, the GRLBM can in principle handle much larger CFL numbers. Indeed, in the tests presented below we employed a CFL coefficient of 0.9 without encountering problems even in diffusive regimes. In addition, in the free-streaming case, the CFL coefficient can be further increased to be up to 1.0.

## 4.2 Numerical Strategy

### 4.2.1 Harmonic Streaming

In what follows, we discuss some of the most subtle issues when developing a numerical infrastructure employing the GRLBM. To this scope, we will restrict ourselves to a 2D scenario with only the position space and frequency shift as this is simpler to explain, visualise, and discuss. However, the same strategy and all conclusions also apply for the velocity space and can be extrapolated to 3D scenarios via the spherical-harmonics decomposition.

$c_k$	Kerr – Schild coordinates			pseudo – Cartesian coordinates		
	$x(\bar{\varphi})$	$y(\bar{\varphi})$	$s(\bar{\varphi})$	$x(\bar{\varphi})$	$y(\bar{\varphi})$	$s(\bar{\varphi})$
$c_0$	2.189220	2.189220	1.410883	2.141385	2.141385	1.414574
$c_1$	-0.063087	0.020200	0.003369	-0.018760	0.016436	0.005429
$c_2$	0.000124	-0.059765	0.004685	0.000000	-0.009044	0.021124
$c_3$	0.000021	-0.000253	-0.006217	-0.000016	-0.000207	-0.000044
$c_4$	0.000392	0.000300	0.018515	0.000235	-0.000112	0.000024
$c_5$	-0.000101	-0.000249	-0.000356	0.000003	-0.000000	0.000000
$c_6$	0.000293	-0.000185	0.000109	0.000000	0.000003	0.000000
$c_7$	-0.000002	0.000005	0.000071			
$c_8$	0.000004	0.000001	0.000058			

**Table 1.** First nine Fourier harmonic-expansion coefficients in a Schwarzschild spacetime in Kerr-Schild coordinates for an emitter at  $x_n^i = (\sqrt{2} + 0.1, \sqrt{2} + 0.1)$ , with  $\Delta t = 0.1$ , using an adaptive RK45 solver.

As mentioned previously, it is numerically not feasible to solve  $N_{\text{grid}} \cdot N_{\text{dir}}$  geodesic equations every time iteration for the streaming step. However, we can drastically reduce the number of ODEs that need to be solved by closely examining the geometric distribution of the directions in which photons propagate from the emitters positions  $x_{d,n-1}^i$  and velocities  $v_{d,n-1}^i$ .

The left panel of Fig. 5 shows the distribution of the photons for an emitter placed at  $x^i = (1, 3, 0)$  outside the event horizon of a Kerr-Schild black hole with  $M = 1$  and  $a = 0$ . Note that in the EF, both the angular distribution and the distribution of the redshift factor  $s$  is far from being the isotropic one expected in flat spacetime and shown with a circle. Rather, it resembles an ellipse and the corresponding distributions are quantified in the three plots in the right panel of Fig. 5, which report the  $x$ ,  $y$  and  $s$  distribution in terms of the emission angle  $\bar{\varphi}$  (in the IF). These distributions vary from point to point and obviously become distorted as one approaches the event horizon. However, given their smooth behaviour it is not difficult to approximate them very accurately with a real Fourier harmonics expansion of the type

$$\chi(\bar{\varphi}) \approx \sum_{\ell=0}^{N_F-1} c_\ell B_\ell(\bar{\varphi}), \quad (91)$$

where

$$B_\ell(\bar{\varphi}) := \begin{cases} 1, & \ell = 0 \\ \sqrt{2} \cos((\ell+1)\bar{\varphi}/2), & \ell = 1, 3, 5, \dots \\ \sqrt{2} \sin(\ell\bar{\varphi}/2), & \ell = 2, 4, 6, \dots \end{cases} \quad (92)$$

$$c_\ell := \langle \chi | B_\ell \rangle = \frac{1}{2\pi} \int_0^{2\pi} \chi(\bar{\varphi}) B_\ell(\bar{\varphi}) d\bar{\varphi}, \quad (93)$$

and, of course, the Fourier basis is orthonormal

$$\langle B_i | B_j \rangle := \frac{1}{2\pi} \int_0^{2\pi} B_i(\bar{\varphi}) B_j(\bar{\varphi}) d\bar{\varphi} = \delta_{ij}. \quad (94)$$

In order to evaluate how many coefficients are necessary for an accurate approximation we consider an extreme scenario in which the emitter is outside but close to the event horizon of a Schwarzschild spacetime in Kerr-Schild coordinates, i.e., at the position  $x_n^i/M = (\sqrt{2}+0.1, \sqrt{2}+0.1)$ , and the timestep is about two orders of magnitude larger than that normally employed in GRMHD simulations, i.e.,  $\Delta t/M = 0.1$ . The first nine coefficients for the Fourier harmonics expansion of  $x(\bar{\varphi})$ ,  $y(\bar{\varphi})$  and  $s(\bar{\varphi})$  for this case are shown in Tab. 1.

As would be expected from the general behaviour shown in the right panel of Fig. 5, we find that the first three coefficients are sufficient to obtain a very good approximation and indeed the coefficients



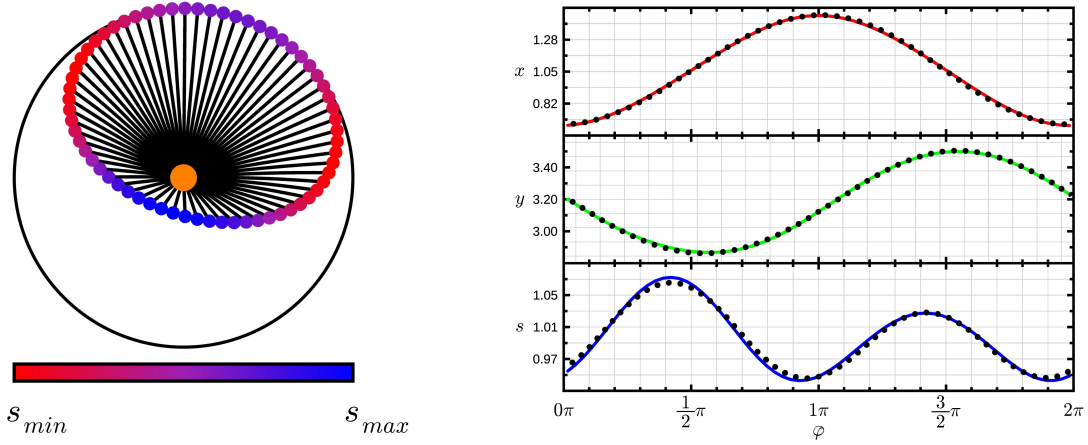


**Figure 5.** *Left panel:* 64 photons emitted from  $x^i = (1, 3, 0)$  (orange dot) and integrated backwards in time for  $\Delta t = 0.5$  in a Kerr-Schild spacetime with  $M = 1$  and  $a = 0$ . The dots around the orange dot show the final positions of the photons after the integration, which correspond to  $x_{d,n-1}^i$ . Their colouring shows their red- and blue-shift. The black circle mark an Euclidean two-sphere with radius  $r = \Delta t = 0.5$ . *Right panel:* The three plots show the final  $x$ ,  $y$ , and  $s$  components depending on the angle of emission  $\varphi$  in the EF. The black dots show instead the reconstruction of the functions from the Fourier transformation of only 5 photons. Note, that the discrepancy between the  $s$  function and the Fourier reconstruction is due to the large timestep  $\Delta t = 0.5$ .

$N_F$	$\epsilon_{\text{rel}}(x)$ [%]	$\epsilon_{\text{rel}}(y)$ [%]	$\epsilon_{\text{rel}}(s)$ [%]
3	0.062347	0.064227	3.707103
5	0.038384	0.041219	0.086021
7	0.000557	0.000547	0.017651
9	0.000395	0.000368	0.001043

**Table 2.** Maximal relative error in emitted  $x_e^i$ ,  $s_e$  values of Fourier expansion in % after streaming for  $\Delta t = 0.1$ . The origin point is  $x_r^i = (\sqrt{2}+0.1, \sqrt{2}+0.1)$  in a Kerr-Schild spacetime with  $M = 1$  and  $a = 0$ .

$c_3$  and higher-order are at least two orders of magnitude smaller in size. Similar estimates apply also for the frequency shift  $s$ , but the more complex dependence in this case requires at least the first five coefficients. A more quantitative measure of the error made can be obtained when comparing the exact values for  $x$ ,  $y$ , and  $s$  for 200 photons with those obtained with different numbers of the Fourier expansion order  $N_F$ , which is reported in Tab. 2. Clearly, the error on the frequency shift is the largest for  $N_F = 3$  and drops significantly when including the next higher-order coefficients. These errors should be considered as upper values, as the match further improves with smaller timesteps  $\Delta t$  and further away from the event horizon.

We should also note that these considerations are also dependent on the spacetime considered and the coordinates employed to describe it, which may or may not be better suited to describe photon motion. For instance, in the case of a Schwarzschild spacetime described in pseudo-Cartesian coordinates (Müller & Grave 2009), the first three Fourier harmonics coefficients would also be sufficient also to accurately capture the frequency shift (see Tab. 1). Overall, we have found that using the first five coefficients  $c_0$ - $c_4$  is sufficient and robust for most cases of interest.

All in all, the Fourier expansion described above has the advantage that instead of solving  $N_{\text{dir}}$  ODEs at every grid-point, we only need to solve  $N_F$  ODEs, which we use to calculate the Fourier coefficients  $c_\ell$  and hence approximate the emitter positions and velocities for all  $N_{\text{dir}}$  photons. In the case of a static spacetime, this procedure only needs to be done once, while the Fourier coefficients must be recalculated at the beginning of every timestep for a dynamical spacetime. In 2D, a Fourier stencil with 5 directions and, therefore 5 Fourier

coefficients is sufficient. In 3D, the same reasoning holds regarding spherical-harmonic coefficients,  $c_{\ell m}$ . Our experience suggests to use a Lebedev-5 stencil (i.e., with  $p_{\text{Leb}} = 5$ ) with 14 directions, which leads to  $((5 + 1)/2)^2 = 9$  spherical-harmonic coefficients ( $\ell = 0, 1, 2, \dots, m \in \{-\ell, \ell\}$ )

$$\chi(\bar{\theta}, \bar{\varphi}) \approx \sum_{\ell=0}^{N_\ell} \sum_{m=-\ell}^{\ell} c_{\ell m} Y_{\ell m}(\bar{\theta}, \bar{\varphi}), \quad (95)$$

Of course, using a different number of ODEs directly impacts the code performance and Fig. 6 is meant to offer a runtime comparison of the four streaming algorithms, namely,

- a flat streaming, without any velocity space interpolation (this is essentially the SRLBM).
- a geodesic streaming, where we solve the geodesic equations for every photon, every timestep.
- a Fourier streaming with static coefficients.
- a Fourier streaming with updating the coefficients every timestep.

A quick look at Fig. 6 is then sufficient to realise that for the reference case of five Fourier coefficients, the harmonic streaming leads to a speedup of a factor of five. Furthermore, it is easy to appreciate that recalculating the Fourier coefficients has only a minor impact on the runtime as most of the extra runtime is spent in evaluating the Fourier transformation (93) and the velocity interpolation. All things considered, the GRLBMRT code using harmonic streaming, is about six times slower than the special-relativistic equivalent. Further profiling tests have shown that roughly 20% of the extra time is spent in the velocity interpolation, while the bulk of the extra run time comes from evaluating the Fourier coefficients. This is also the reason why it is essential to use the lowest number of Fourier coefficients.

#### 4.2.2 Adaptive stencil

Quite generically, the optically thin regime is the most challenging for LBMs. This is true in special relativity and is made worse in curved spacetimes. This is because, without sufficient fluid scattering, the discretized intensities are not redistributed enough, which leads to beam separation (see, for instance, the top left panel in left part of

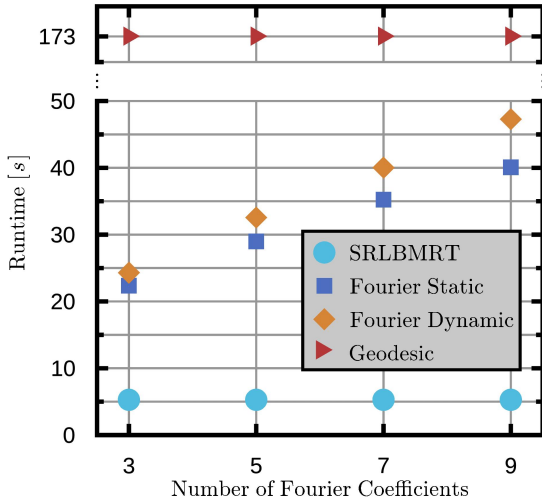


**Figure 6.** Total runtime in seconds as a function of the Fourier coefficients  $N_F$  using a stencil with  $N_{\text{dir}} = 200$  populations on a  $200 \times 250$  Cartesian grid. The background spacetime is that of a Schwarzschild black hole in Kerr-Schild coordinates and the evolution was carried out till  $t = 5.1 M$  with a timestep of  $\Delta t = 0.015$  using an adaptive RK45 solver for the solution of the geodesic equations (31)-(33).

Fig. 8). Obviously, it is possible to increase the directional resolution to improve this behaviour, but given long enough free-streaming paths, beam separation will tend to occur. To resolve some of these issues, we have introduced an adaptive stencil whereby at each grid-point we properly orient the stencils to capture the directions in which most of the photon bundles propagate. This improves significantly the directional resolution and hence the handling of the optically thin regime with the GRLBM.

More specifically, in our adaptive stencil we start from considering the basic Fourier and Lebedev stencil we have already discussed and we then introduce additional ghost intensities in the “forward” direction of the stencil (see Fig. 7 for a diagrammatic representation).

In 2D, the forward direction is defined by a vanishing polar angle,  $\phi = 0$  and ghost directions are added following to the distribution  $D(\phi) = \arccos(1 - 2\phi)/\pi$  in the interval  $\pm\pi/8$  around the forward direction. The function  $D(\phi)$  essentially provides a distribution of directions that is not isotropic, concentrating the stencils around the forward direction. Using this distribution, we determine how many ghost directions need to be added between two existing directions and we then arrange all ghost directions between two directions uniformly for the quadratic velocity- interpolation scheme (see left panel of Fig. 7 for a schematic representation).

In 3D, the logic is very similar and we define the forward direction by a vanishing azimuthal angle,  $\theta = 0$  and introduce two refinement levels (these are shown with light-blue and dark-blue shaded regions in the right panel of Fig. 7). We then add a ghost direction at the center of every triangle whose center lies within the light-blue refinement level, while in the dark-blue refinement level we add the center of each triangle edge, thus adding three ghost directions. The two refinement levels can be used exclusively or layered inside each other (see the right panel of Fig. 7).

Referring to the original directions as to the “real” directions, the counting of direction is then simply given by  $N_{\text{pop}} = N_{\text{real}} + N_{\text{ghost}}$ , where the ghost directions have quadrature weights of  $w_d = 0$  and do not contribute to the numerical integrals. However, they contribute to the streaming step by improving the accuracy of the velocity

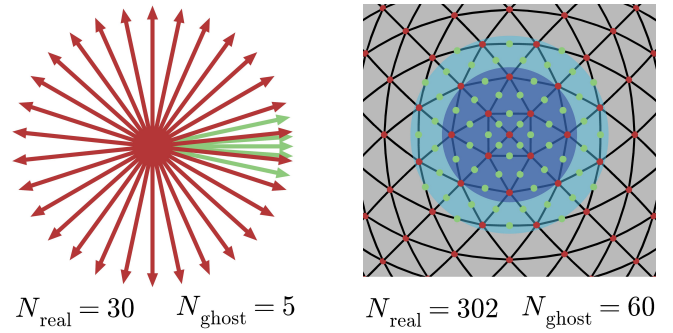


**Figure 7.** *Left Panel:* Two-dimensional adaptive stencil with 30 real (red arrows) and five ghost (green arrows) directions. *Right Panel:* North pole of a three-dimensional adaptive stencil with two refinement levels (blue shadings). Shown in red are the real directions, while green is used for the ghost directions.

interpolation in the forward direction and the corresponding flux. In addition, we allow the stencil to rotate and align its refined forward direction with the flux (see Appendix D for details). We also define a proper naming convention to express the various options of the adaptive stencils. More specifically, a 2D adaptive stencil is named after the number of real directions (same as the order of stencil) and the number of ghost directions, so that, for instance, the stencil in the left panel of Fig. 7 is the Fourier-30-5. Similarly, the naming notation of the adaptive 3D stencils is given by listing the refinement levels from low to high in terms of  $\pi$ , so that, for example, the adaptive stencil shown in the right panel of Fig. 7 is referred to as Lebedev-29-0.15-0.1, with the first refinement level at  $0.15\pi$ , and the second level at  $0.1\pi$ .

While the advantages in terms of direction resolution offered by the adaptive stencil are obvious, a final remark should be made on the related additional costs. Within a GRLBM scheme, where the velocity interpolation is already intrinsically present, the use of adaptive stencils does not lead to any significant additional computational cost. This is not the case for the SRLBM scheme, where we would need to introduce a velocity interpolation, drastically impacting the computational complexity. A more detailed cost analysis can be found in Section 5.3.

## 5 NUMERICAL TESTS

This section is dedicated to the presentation of a series of standard and non-standard tests in 2D and 3D aimed at validating the correctness of the GRLBM described above and to measure its performance and a variety of conditions and choices for the stencil order. We will start with considering the flat-spacetime tests by Weih et al. (2020c) and then move on to curved (but fixed) spacetimes. For consistency, we set the CFL factor to 0.9 for all tests presented here.

### 5.1 Flat Spacetime Tests

#### 5.1.1 Sphere Wave

This test consists of a spherical light pulse propagating radially outwards in flat spacetime with initial data given by  $E = 1$  and  $F^i = 0$  inside a sphere of radius  $r \leq 0.1$ . The top panel of Fig. 8 reports the results of 2D calculations at  $t = 0.7$ , with the different sub-panels reporting the results for different combination of the real and ghost directions  $N_{\text{real}}$  and  $N_{\text{ghost}}$  (we report a single quadrant but the calculations do not enforce any symmetry). When concentrating on the

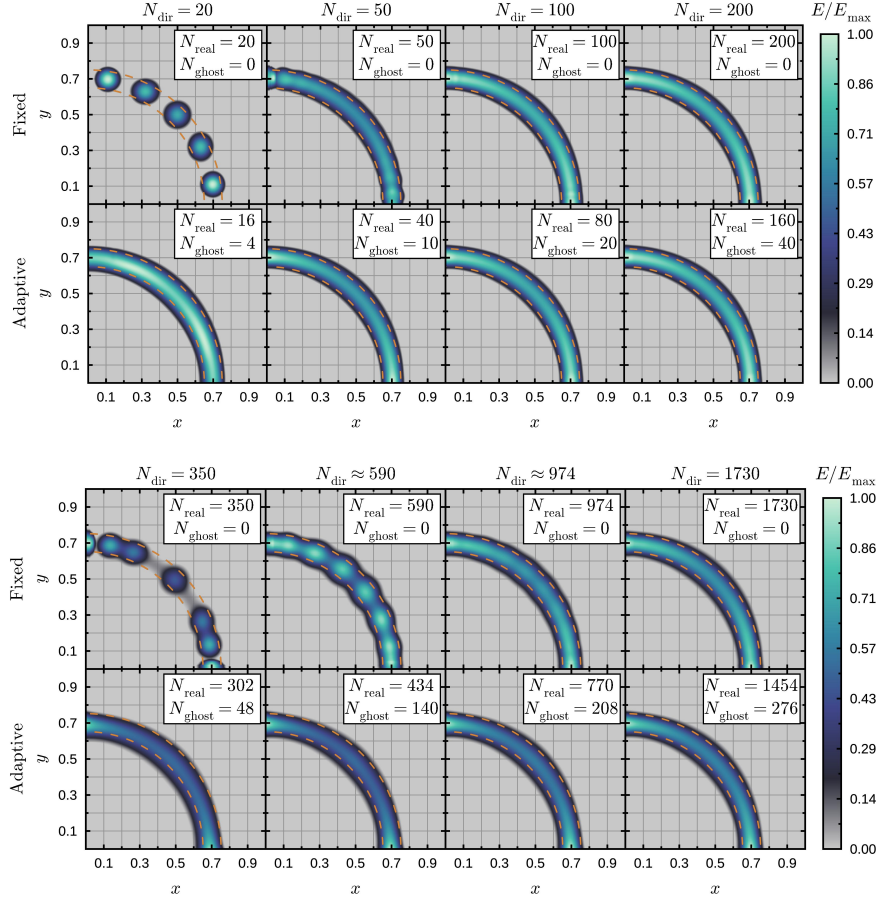


**Figure 8.** *Top panel:* Energy distribution for the 2D sphere-wave test  $t = 0.7$ . The top panels report the results for fixed-streaming stencils ( $N_{\text{ghost}} = 0$ ) for increasing number of directions ( $N_{\text{real}}$ ) from left to right. The bottom panels, on the other hand, show the results when employing adaptive-streaming stencils with the same number of total directions ( $N_{\text{dir}}$ ) matching the top panels and highlighting that fewer directions are sufficient to obtain comparable solutions. The grid has extent  $x, y \in [-1, 1]$  with  $dx = dy = 0.006$  ( $300^2$  grid-points) and a timestep  $dt = 0.006$ . Adaptive streaming uses 20% ghost directions. *Bottom panel:* The same as top panel but at  $z = 0$  of a 3D simulation with  $x, y, z \in [-0.9, 0.9]$ ,  $dx = dy = dz = 0.01$  ( $180^3$  grid-points), and  $dt = 0.009$ . In both panels, The orange dashed lines indicate the analytical position of the sphere wave.

top portion with fixed (or uniform) stencil ( $N_{\text{ghost}} = 0$ ), it is possible to note that beam separation occurs when using 20 or 50 real directions. Increasing them to 100 directions leads to an improvement, but artefacts in the energy distribution can still be found right next to the coordinate axes. Such artefacts, which are due to the spatial interpolation being trivial along the principal directions, can be further moderated when using 200 directions, which leads to a propagating shell that is mostly uniform in the polar direction. When using the adaptive stencil, as shown in the bottom portion of the top panel of Fig. 8, we obtain a uniform propagating shell already with only  $N_{\text{real}} = 16$  and  $N_{\text{ghost}} = 4$  the quality of the result increases as  $N_{\text{real}}$  and  $N_{\text{ghost}}$  are increased. The improvements tend to saturate between 100 and 200 directions and going beyond 200 directions does not improve the results significantly.

The bottom panel of Fig. 8 reports the equivalent results of 3D calculations restricted to the plane with  $z = 0$ , where it is possible to appreciate that the beam separation with the fixed stencil (top sub-panels) is more pronounced and still clearly visible with 590 directions. Overall, also in 3D, the adaptive stencil and the addition of ghost directions (bottom sub-panels) produces a much smoother and homogeneous distribution of the energy density, while retaining the error along the principal directions. Since the interpolation is intrinsically more diffusive in 3D while it remains very accurate near the

coordinate axes, it is not surprising that the accumulation of energy along these axes is even more pronounced in the 3D simulations. All in all, this test in the free-streaming regime shows that the adaptive stencil provides a significant improvement over the fixed stencil: it yields the needed isotropy and reduces the computational costs.

### 5.1.2 Shadow Casting

For the following test, we use the same initial data but keep the intensities in the sphere of radius  $r_s < 0.1$  fixed to the initial values, giving a constant emitting light source similar to a star. We also introduce an optically thick sphere of radius  $r_p = 0.25$  at position  $(x_p, y_p, z_p) = (0.75, 0.75, 0.00)$ , with an absorption coefficient  $\kappa_a = 10^{10}$ , effectively absorbing all radiation.

Figure 9 shows the results for the 2D and 3D simulations, respectively. Note how in the 2D case (top panels), a shadow is cast downstream of the sphere, while elsewhere the energy density falls-off like  $1/r$ , as expected. Furthermore, when using a fixed stencil (top portion of the top panel), it is possible to notice evident beam-separation artefacts when using only 50 directions, but also that these are considerably suppressed when increasing to 100 directions, leaving some inaccuracies only along the principal directions when using

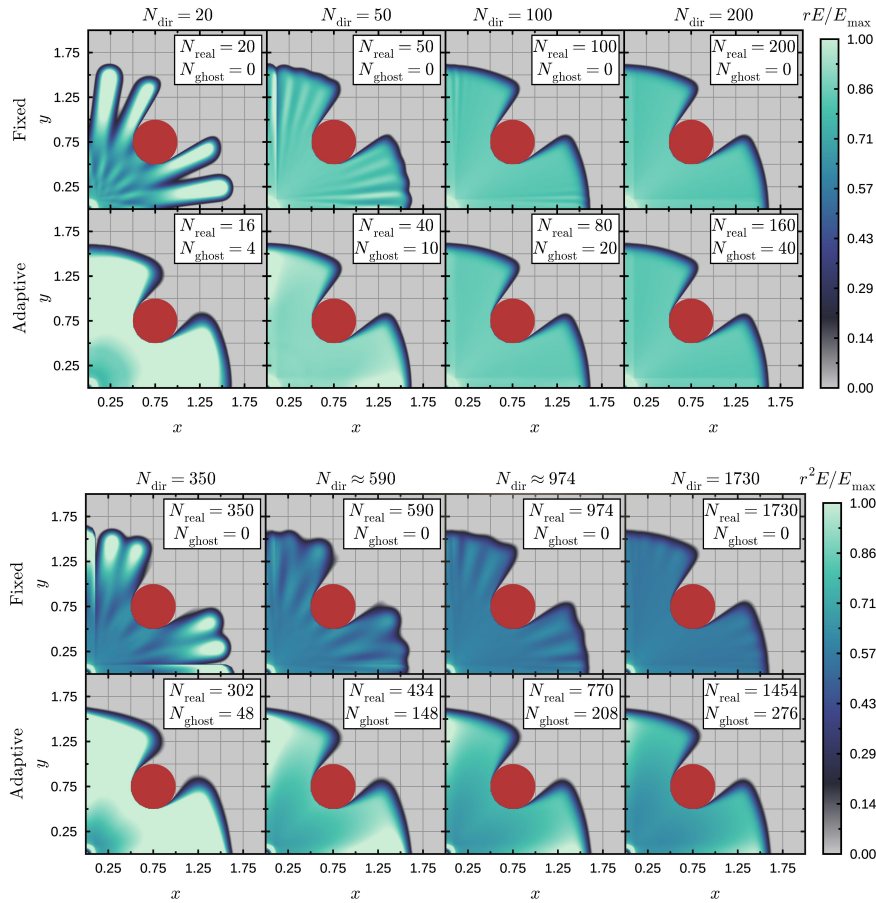


**Figure 9.** The same as in Fig. 8 but for the shadow-casting problem at  $t = 1.5$  and where the colormap reports the rescaled energy density, i.e.,  $rE$  ( $r^2E$ ) so that the solution should be constant in 2D (3D). The 2D data (top panel) refers to a grid with  $x, y \in [-0.2, 1.7]$ ,  $dx = dy = 0.01$  ( $190^2$  grid-points), and  $dt = 0.009$ . The 3D data (bottom panel), on the other hand, refers to a grid with  $x, y, z \in [-0.2, 1.7]$ ,  $dx = dy = dz = 0.01$  ( $190^3$  grid-points), and  $dt = 0.009$ . In all cases, the red-filled circle indicates the position of the sphere casting the shadow.

200 directions. At the same time, the shadow cast when employing the adaptive streaming (bottom portion of the top panel) is already very sharp with only  $N_{\text{real}} = 40$  and  $N_{\text{ghost}} = 10$  directions and the solution further improves with 100 directions, being comparable to that with twice as many fixed directions and saturating after that.

When considering the 3D simulations (bottom panels), this test shows all of its complexity and challenges when using a fixed stencil. While a shadow is cast already with few directions, the quality of the energy-density solution is poor and does not improve significantly when doubling the number of directions. With adaptive streaming, the shadow casting is much better, but the inverse square law seems broken due to the more substantial bias toward the principal directions. In Sec. 5.1.4, we will look closer at the inverse square law and see that the discrepancy is not as severe as it might seem.

### 5.1.3 Beam Crossing

While the two previous tests provide ideal testbeds to highlight the advantages of the adaptive stencil, due to most of the light at one grid cell moving in the same direction, this is not the case for another standard test, namely, the beam-crossing test. We recall that this test amounts to evolving two beams of radiations along directions that eventually cross and interact leading to a local increase in the energy density. After the crossing, the two beams should continue

their motion along the initial direction of propagation, but this is not always reproduced by radiative-transfer approaches, for which this represents a very challenging test. A classical example of this failure is given by the M1-moment scheme, where the photon momenta are actually linearly combined and after the crossing a single beam is produced propagating in the combined direction. Indeed, the ability of successfully perform this test has been reported only for more advanced approaches, such as the SRLBM (Weih et al. 2020c) or MonteCarlo approaches (Foucart 2018).

We set up two mono-directional constantly emitting beams with the same energy density  $E = 1$  and flux density norm  $|F^i| = 1$ . The beams are emitted at the boundary cells where  $x = -0.5$ , with a flux direction of components  $(0.3, 0.1)$  and  $(0.3, -0.1)$  between  $y \in [-0.2, -0.15]$  and  $y \in [0.15, 0.2]$  respectively. Note that the initial data is not identical for all the stencil configurations. When using the adaptive stencil, a delta-like intensity distribution where only a single direction holds any intensity while all others are zero leads to high interpolation errors in velocity space. Depending on the resolution, each stencil has its own maximal intensity distribution, and therefore a maximum value of  $|F^i|$  it can resolve without interpolation errors becoming too big (see Appendix D for a detailed discussion of this issue). As a result, higher-order stencils, especially stencils with more ghost directions and/or higher levels of refinement, have a higher initial flux density. This artificial maximum flux boundary does not

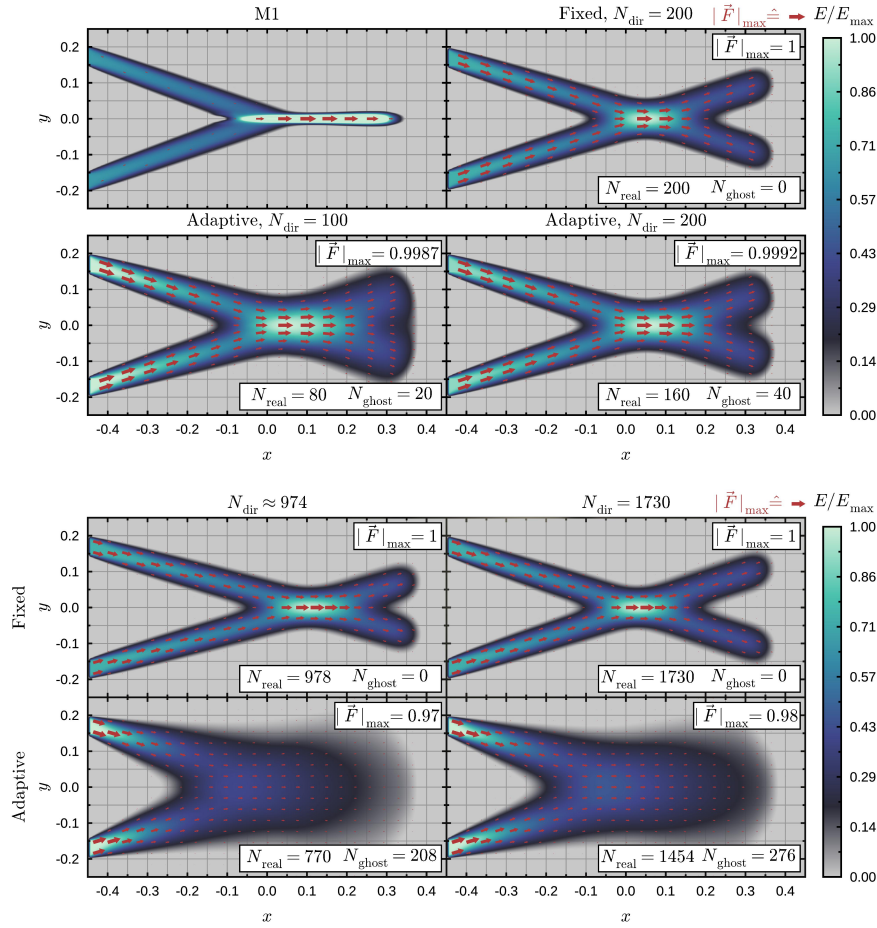


**Figure 10.** The same as in Fig. 8 but for the beam-crossing problem at  $t = 0.85$ . The top-left panel reports the solution with the M1 approach, which obviously fails in this test. The 2D data (top panel) refers to a grid with  $x \in [-0.5, 0.5]$ ,  $y \in [-0.25, 0.25]$ ,  $dx = dy = 0.005$  ( $200 \times 100$  grid-points), and  $dt = 0.0045$ . The 3D data (bottom panel), on the other hand, refers to a grid with  $x \in [-0.5, 0.5]$ ,  $y \in [-0.25, 0.25]$ ,  $z \in [-0.125, 0.125]$ ,  $dx = dy = dz = 0.005$  ( $200 \times 100 \times 50$  grid-points), and  $dt = 0.0045$ .

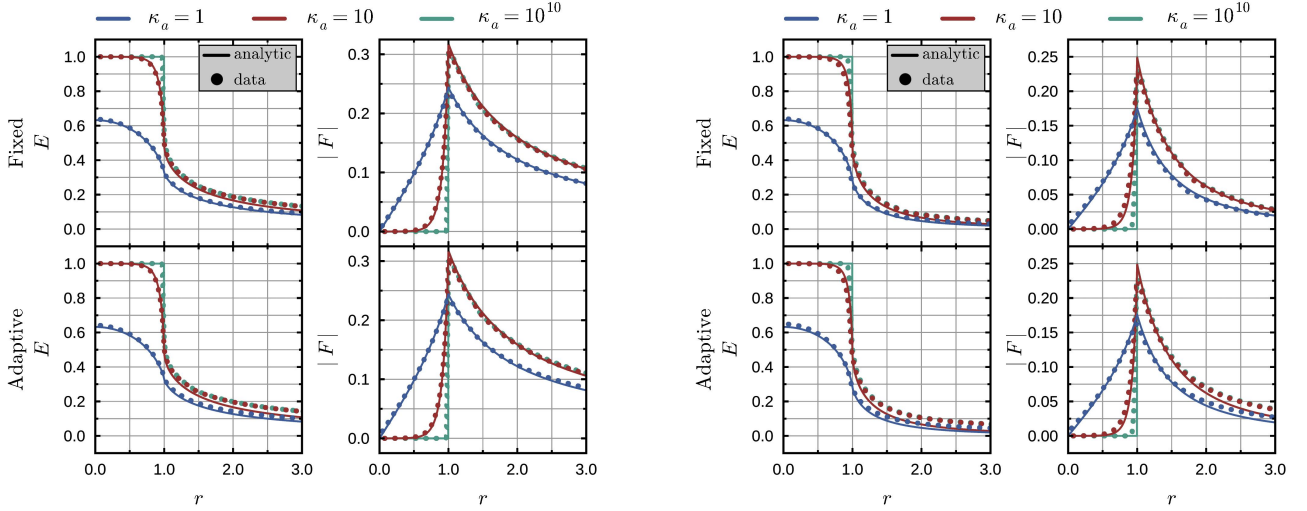
limit the fixed streaming method. Instead, we find the direction vector closest to the desired direction in our stencil and set the corresponding intensity to one and all others to zero.

Figure 10 shows the results of the beam-crossing test, again reporting the outcome of the 2D simulations in the top panels and those of the 3D simulations in the bottom panel. Concentrating on the former first, we show in the top-left sub-panel the solution obtained with the M1-moment scheme as computed by Weih et al. (2020c). Note how after the crossing the two beams merge into one, therefore failing the test. The remaining sub-panels on the top of Fig. 10 show the results of our novel GRLBM, with the top-right one being with a fixed stencil and the bottom sub-panels showing the results with adaptive stencils. Clearly, in all cases the test is passed already with  $N_{\text{real}} = 80$ ,  $N_{\text{ghost}} = 20$  directions and the solution improves as the number of directions is increased.

The bottom panel of Fig. 10 shows instead the results in 3D which are much poorer and that the velocity-space resolution is too low to resolve sharp, distinct beams with the adaptive approach. Indeed, even with an adaptive Lebedev stencil of order  $p_{\text{Leb}} = 65$  with 1454 real and 276 ghost directions, the diffusion is so pronounced that the beams hardly cross. We believe this behaviour is mostly the result of the “mono-directional” prescription in which our adaptive stencil is implemented. More precisely, in the present approach the adaptive stencils aligned naturally along the direction of propagation of the

radiation, which is assumed to be only one. Since before crossing there is a single direction of propagation for each beam, the adaptive approach works very well and leads to two distinct and sharp beams. At the crossing, however, the radiation field will have two distinct directions of propagation and the mono-directional adaptive stencil will adapt to their average, leading to a wrong alignment. As a result the stencil has less resolution in the beam directions, which leads to additional numerical diffusion in the velocity space interpolation.

While this phenomenology indicates that the use of a mono-directional adaptive stencil is not satisfactory in conditions where the radiation is not propagating along a main direction, it also provides a useful hint on how to improve it. In particular, much of the diffusion can be removed by making the adaptive stencil even more adaptive in at least two different ways. First, a new implementation can be made in which the adaptive stencil is either “switched” on or off depending on the local conditions of the radiation field. Second, a different approach could consist in decomposing the angular distribution intensity more finely and set the adaptive stencil not to follow a single direction but the two directions in which the angular distribution of the intensity is peaked. This would essentially transform the mono-directional adaptive stencil developed here into a multi-directional one. Since these algorithmic modifications affect a considerable part of the numerical infrastructure, we have decided to explore this possibility in future work.



**Figure 11.** Results of the radiating-sphere test reporting with filled circles of different colours the numerical 1D profiles for the energy (left part) and the flux density (right part) for different values of  $\kappa_a = \eta$ ; shown with solid lines are the corresponding analytic solutions. Both in the left and in the right panels, the top sub-plots refer to the fixed streaming, while the bottom ones to the adaptive streaming. The 2D data (left panel) refers to a grid with  $x, y \in [-4, 4]$ ,  $dx = dy = 0.02$  ( $400^2$  grid points), and  $dt = 0.018$ . The 3D data (right panel), on the other hand, refers to a grid with  $x, y, z \in [-4, 4]$ ,  $dx = dy = dz = 0.05$  ( $160^3$  grid points), and  $dt = 0.045$ .

#### 5.1.4 Radiating Sphere

The next test corresponds to a dense sphere with a sharp boundary to vacuum, radiating constantly and homogeneously from its surface [Smit et al. \(1997\)](#). Hence, as initial data we set the emissivity and absorption opacity to be constant and equal  $\eta = \kappa_a$  inside a sphere of radius  $r < 1$ . Eventually, this system will reach a steady state for which the analytic solution for the distribution function is

$$f(r, \mu) = 1 - \exp \left[ -\kappa_a \left( r\mu + \sqrt{1 - r^2(1 - \mu^2)} \right) \right], \quad (96)$$

and

$$f(r, \mu) = 1 - \exp \left[ -2\kappa_a \sqrt{1 - r^2(1 - \mu^2)} \right], \quad (97)$$

for  $r < 1, \mu \in [-1, 1]$  and for  $r \geq 1, \mu \in [\sqrt{1 - 1/r^2}, 1]$ , respectively, and where  $\mu := \cos \theta$ . The moments can then be computed by integrating the distribution functions and are given by

$$E(r) = \frac{1}{\pi} \int_{\mu_{\min}}^{\mu_{\max}} \frac{f(r, \mu)}{\sqrt{1 - \mu^2}} d\mu, \quad F(r) = \frac{1}{\pi} \int_{\mu_{\min}}^{\mu_{\max}} \frac{\mu f(r, \mu)}{\sqrt{1 - \mu^2}} d\mu, \quad (98)$$

and

$$E(r) = \frac{1}{2} \int_{\mu_{\min}}^{\mu_{\max}} f(r, \mu) d\mu, \quad F(r) = \frac{1}{2} \int_{\mu_{\min}}^{\mu_{\max}} \mu f(r, \mu) d\mu, \quad (99)$$

in 2D and 3D, respectively.

Figure 11 shows the results for the 2D (filled circles in the left panels) and 3D simulations (filled circles in the right panels) for different values of the absorption opacity. In both cases, the numerical results closely follow the analytical solution (solid lines of different colour) inside the radiating sphere where  $\kappa_a = \eta \neq 0$ , with relative errors in the energy density below 0.0062% (0.023%) and flux density below 0.234% (0.233%) with the fixed (adaptive) stencil. Outside the sphere, in the free-streaming region, both methods tend to have an energy density that is slightly larger than the analytical one. The error is smaller for the fixed stencil than for the adaptive stencil 1.06% and 1.81% respectively. A similar behaviour is shown also by the

flux density, that has a smaller error with the fixed stencil, while the adaptive approach overshoots slightly, although the relative error is 0.043% and 0.046% respectively. Very similar behaviours are shown also in the case of full 3D simulations, where the relative errors are slightly larger but mostly because of the smaller spatial resolution, i.e.,  $160^3$  grid-points to be contrasted with the  $400^2$  grid-points of the 2D simulations.

Overall, this test shows that both the fixed and the adaptive stencil produce correct and accurate results in optically intermediate to thick regimes. It also demonstrates that the fixed stencil is more accurate in the free-streaming limit than the adaptive counterpart both in 2D and in 3D at least in scenarios with very high symmetry, as the one considered here. Under more general conditions, however, we expect the adaptive stencil to provide comparable if not better accuracy.

#### 5.1.5 Static and boosted diffusion

So far, all our tests have only tested pure streaming, absorption, and emission. To properly test if the collision step still behaves correctly even with the addition of ghost directions, we test the scattering regime in the diffusive limit of the radiative-transfer equation. Following the standard approach for a static diffusion test ([Pons et al. 2000](#); [Kuroda et al. 2016](#); [Weih et al. 2020b](#); [Radice et al. 2022](#)), we set our initial data for the energy density to a Gaussian according to the analytical solution at  $t_0 = 1$

$$E(r, t) = t^{-d/2} \exp \left( -\frac{r^2}{4\mathcal{D}t} \right), \quad (100)$$

$$F(r, t) = \frac{rE}{2t(1 + a\mathcal{P}e)}, \quad (101)$$

$$\mathcal{D} = \frac{1}{d\kappa_0} (1 + a\mathcal{P}e), \quad (102)$$

where  $\mathcal{D}$  is the diffusion coefficient and includes corrections for additional numerical diffusion proportional to the Péclet number  $\mathcal{P}e$ , where  $a = 0.64$  ( $a = 0.75$ ) in 2D (3D) simulations, and  $d \in \{2, 3\}$  the number of spatial dimensions.

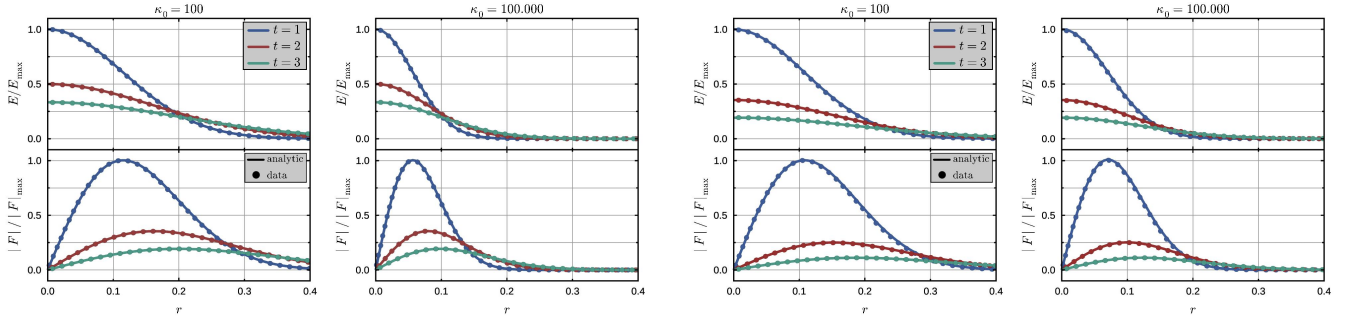


**Figure 12.** Shown in the left and right panels are the energy density (top rows) and flux density (bottom rows) of the radiation-diffusion test at times  $t = 1, 2, 3$ ; numerical data is shown with filled circles, while solid lines are used for the analytic solution. For each panel, the left (right) column refers to an opacity  $\kappa_0 = 10^2$  ( $\kappa_0 = 10^5$ ); absorption, emission, and forward scattering are set to zero  $\kappa_a = \eta = \kappa_1 = 0$ . The left panel refers to 2D simulations on a grid with  $x, y \in [-0.5, 0.5]$ ,  $dx = dy = 0.005$  ( $200^2$  grid-points), and  $dt = 0.0045$ , while the right panel reports the results of the 3D simulations on a grid with  $x, y, z \in [-0.5, 0.5]$ ,  $dx = dy = dz = 0.01$  ( $100^3$  grid-points), and  $dt = 0.0009$ . Because of the different resolutions, the 2D and 3D results refer to  $\mathcal{P}e = 1$  (left column),  $\mathcal{P}e = 1000$  (right column) and  $\mathcal{P}e = 0.5$  (left column),  $\mathcal{P}e = 500$  (right column), respectively.

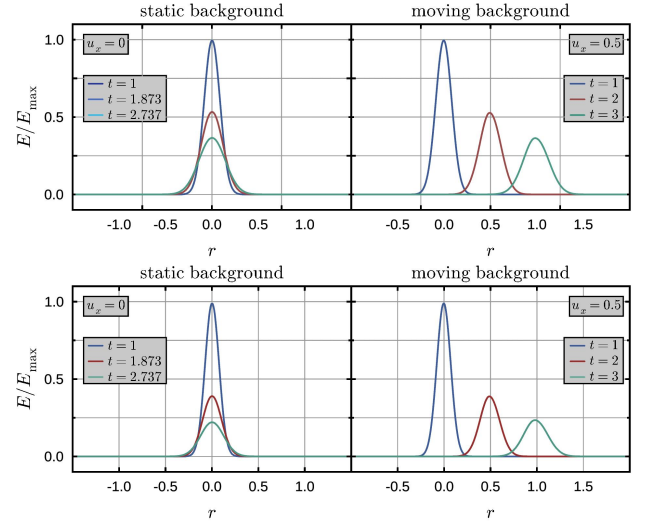
The diffusion test is also the first instance in which the Lambda-Iteration in the collision step [see Eq. (55) and related discussion] has to be employed and iterated for multiple steps. In the most extreme case, i.e., of a 3D simulation with  $\kappa_0 = 10^5$ , we measured a maximum number of 100 and an average of 3.69 iteration steps per timestep; for all other simulations, we measure smaller values both the maximum and the average number of iteration steps. It is also worth remarking that our initial-data approach only sets a value for the energy and flux density, with no control over the pressure tensor  $P^{ij}$ , which is calculated after the first iteration (see Appendix D for details). As a result, the initial value of the pressure are “inconsistent” with the prescriptions of  $E$  and  $F$  and the first couple of timesteps are needed to drive the pressure tensor to consistent values. As a result, the initial steps are also those where the number of steps in the Lambda-iteration is the largest, dropping drastically once the pressure is consistently computed.

Figure 12 shows the evolution of the energy and flux density of the static-diffusion test either in 2D (left panel) or in 3D (right panel), reporting with filled circles the numerical solutions and with solid lines of the same colour the corresponding analytic solutions. All results refer to the adaptive-streaming approach and show that numerical values match the analytical solution very well, even for the extreme case of  $\kappa_0 = 10^5$ , with a maximum relative error of 0.016%. Not shown in Figure 12 are the results when employing the fixed-streaming approach, as the results look indistinguishable from the adaptive streaming and the relative error is of the same order.

A more challenging diffusion test can be made when considering the diffusion in a moving medium. In this case, we follow Radice et al. (2022) and Musolino & Rezzolla (2024), and repeat the diffusion test in a moving background fluid with  $u_x = 0.5$ . For the initial data at  $t = 1$ , we use the same energy and flux density as in the previous diffusion test and to account for the moving fluid, we need to Lorentz-boost the initial energy-momentum tensor  $\tilde{T}^{\mu\nu}$  from the FF to the LF with  $T^{\mu\nu}$ . Since we need the entire energy momentum tensor, we also require the (isotropic) pressure in the FF, which takes the diagonal form  $\tilde{P}^{ij}/\tilde{E} = \delta^{ij}/\mathcal{D}$  in the diffusive limit. Considering the additional numerical diffusion, this leads to the following pressure tensor

$$\tilde{p}^{ij} = \frac{\tilde{E}}{\mathcal{D}(1 + a \mathcal{P}e)} \delta^{ij}. \quad (103)$$

Note that time dilation in terms of the inverse Lorentz factor  $\gamma^{-1} =$



**Figure 13.** Moving radiation-diffusion test at three different times and  $\kappa_0 = 1000$ ; the left columns report the values of the normalised energy density in the FF (where the fluid is at rest  $u_x = 0$ ) while the right columns those in the LF (where the fluid moves with  $u_x = 0.5$ ). The top panel refers to the 2D simulations on a grid with  $x \in [-1, 2]$ ,  $y \in [-0.5, 0.5]$ ,  $dx = dy = 0.001$  ( $300 \times 100$  grid-points), and  $dt = 0.0009$ , while the bottom panel to the 3D data on a grid with  $x \in [-1, 2]$ ,  $y, z \in [-0.5, 0.5]$ ,  $dx = dy = 0.001$  ( $300 \times 100^2$  grid-points), and  $dt = 0.0009$ .

$\sqrt{1 - u_x^2} = 0.866$  needs to be taken into account when comparing the results in the LF and in the FF.

Figure 13 shows that the results of the boosted diffusion test (right panel) with adaptive streaming and compares it with the results of the static case. Obviously, in the former case, the energy density is both diffused and advected at the expected rate, i.e., by 0.5 space units per time units. When comparing the height of the Gaussian peaks, it is possible to see they are very similar, with the energy being slightly smaller in the case of the boosted diffusion most likely as a result of the errors introduced by the Lambda-Iteration scheme. At any rate, the relative difference between the two solutions is very small and below 0.8%; a similar behaviour has been observed also with the fixed stencils and is not reported in Fig. 13.

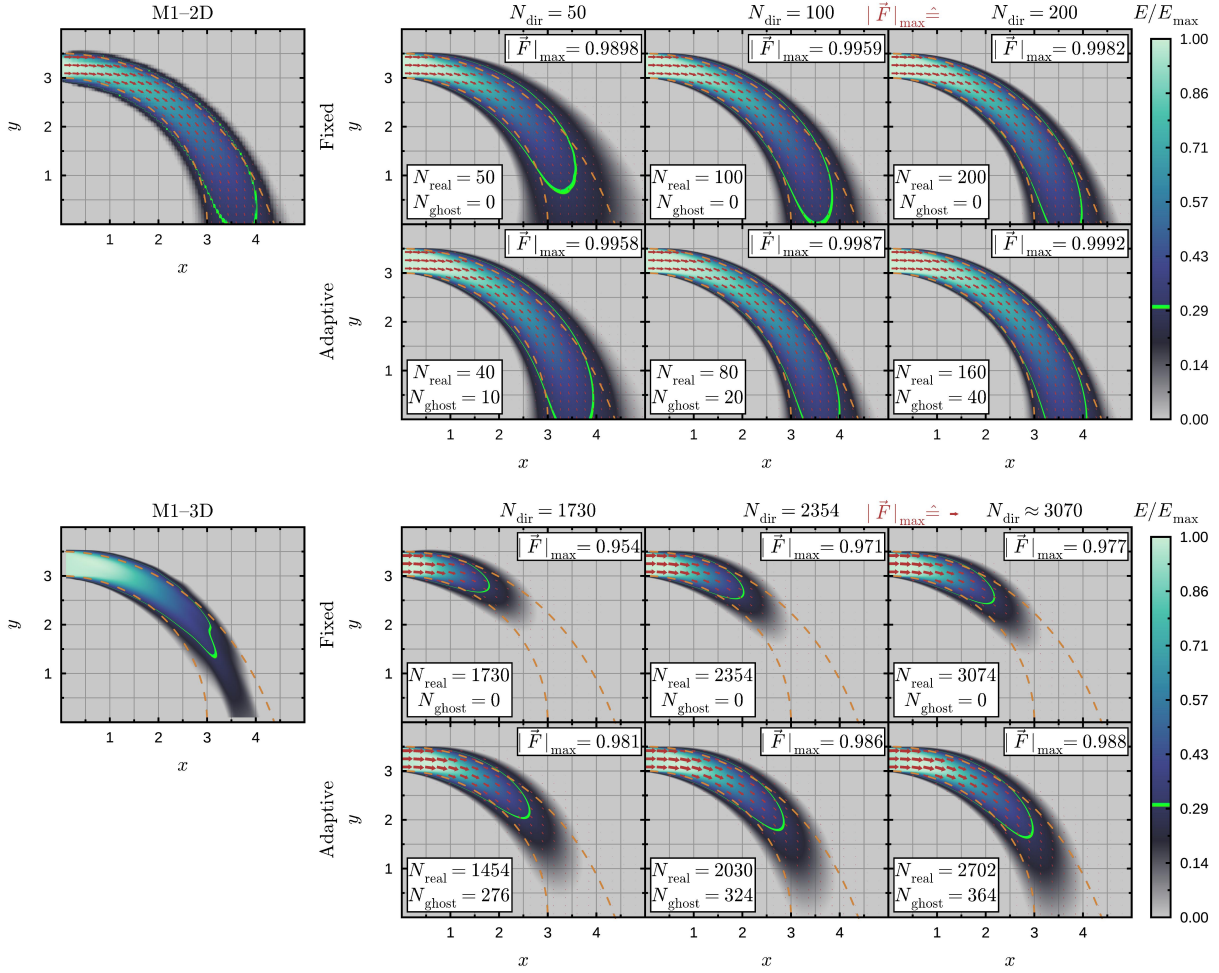


**Figure 14.** Normalised energy density in a vacuum curved-beam test at  $t = 10M$  in a Schwarzschild spacetime expressed Cartesian Kerr-Schild coordinates. The orange dashed lines show the trajectories of the bounding geodesics, while the bright-green region in the colormaps marks the range  $0.29 - 0.30$  to highlight the progression of the beam. The top panel reports the 2D data on a grid with  $x \in [0, 5]$ ,  $y \in [0, 4]$ ,  $dx = dy = 0.02$  ( $250 \times 200$  grid-points), and  $dt = 0.018$ . The bottom panel, on the other hand, refers to the 3D data computed on a grid  $x \in [0, 5]$ ,  $y \in [0, 4]$ ,  $z \in [-0.25, 0.25]$ ,  $dx = dy = dz = 0.025$  ( $200 \times 160 \times 20$  grid-points), and  $dt = 0.0225$ . In both panels, the top rows report the data with either a fixed or adaptive stencils, respectively, while the top-left sub-panels offer as comparison with the solution computed with the M1 method, either in 2D (top panel, [Weih et al. 2020a](#)), or in 3D by (bottom panel, [Musolino & Rezzolla 2024](#)).

## 5.2 Curved Spacetime Tests

### 5.2.1 Curved Beam

We now turn our attention to tests in curved spacetimes and thus validating the code in the solution of the newly derived equations (84) and (86). The first of these tests is the well-known “curved beam” test, consisting in the emission of a beam of radiation close but outside of the unstable radial photon orbit of a Schwarzschild black hole (we recall that this orbit is at  $r = 3M$  for a black hole of mass  $M$ ). The behaviour expected in this test is that the beam of radiation will not propagate unchanged on a straight line, but will instead be “bent”, suffer diffusion, and redshift.

For this test, we use a Cartesian Kerr-Schild Metric with  $M = 1$  and  $a = 0$  with a surrounding vacuum, i.e.,  $\kappa_0 = \kappa_1 = \kappa_a = \eta = 0$ . For the initial data, both in the 2D and 3D simulations, we set the energy density to 1 and the flux density towards the positive  $x$ -direction in the LF to have norm 1. In 2D, this is done at  $x/M = 0$  and at  $y/M \in [3, 3.5]$ , while in 3D, the beam has a square section initially placed at  $y/M \in [3, 3.5]$  and  $z/M \in [3, 3.5]$ .

Figure 14 shows the results with the 2D (top series of panels) and with the 3D simulations (bottom series of panels); furthermore, in each case the upper part reports the results with the fixed stencils, while the lower part refers to the adaptive-stencil approach, and the top-left sub-panels show a comparison to the M1 method, either in 2D (top panel, [Weih et al. 2020a](#)), or in 3D by (bottom panel, [Musolino & Rezzolla 2024](#)). Starting with the 2D results Fig. 14 highlights that when using 200 directions and a fixed stencil, the results of the GRLBM are comparable or better than those obtained with the M1 method. This can be best appreciated when concentrating of the width of the region in bright green, which marks a special position in the colormap and that we use to mark the propagation of the beam. Interestingly, this test shows more than others the advantage of the adaptive stencil, which produces comparable results already with 100 directions and provides remarkably good results already with only 50 directions.

When considering the simulations in 3D, the results shown in the bottom panel of Fig. 14 that using a sufficient number of direction leads to a beam propagation that suffers only mildly of diffusion at



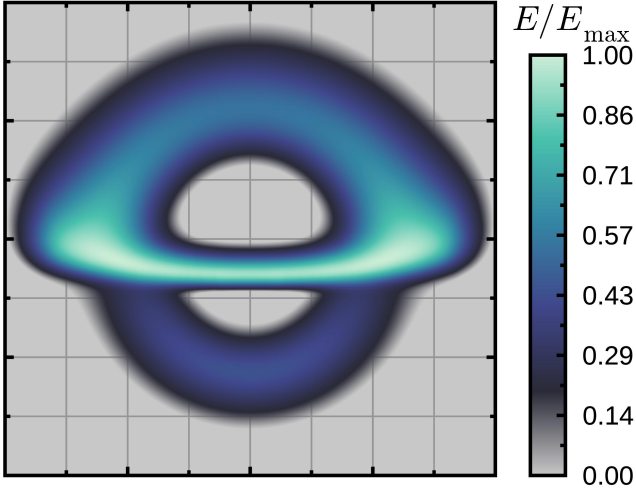


**Figure 15.** Normalised energy density from a thin disc around a Schwarzschild black hole in Cartesian Kerr-Schild coordinates on a grid with  $x \in [-14, 14]$ ,  $y \in [-10, 15]$ ,  $z \in [-18, 14]$ ,  $dx = dy = dz = 0.166667$  ( $171 \times 153 \times 195$  grid-points), and  $dt = 0.15$ . The data refers to a fixed stencil with a Lebedev order of  $p_{\text{Leb}} = 65$  (1454 directions).

the edges and that the shape of the beam is closer to the expected one than with the M1 method, where the tendency to focusing, already encountered in the beam-crossing test, is present. Furthermore, these considerations apply both in the case of fixed stencils (top part) and of the adaptive one, although the latter shows an overall better performance. In summary, also the results of the curved-beam tests clearly indicate the ability of the GRLBM to handle the propagation of radiation in the free-streaming regime accurately and with minor diffusion also in the presence on spacetimes in strong curvature.

### 5.2.2 Lensed thin disc around a black hole

As our final test, we consider a somewhat different setup and present a novel test that could be employed when considering novel methods handling radiative-transfer problems in curved spacetimes. In particular, following the recent work of the Event Horizon Telescope collaboration on the imaging of supermassive black holes (Akiyama & et al. 2019a; Event Horizon Telescope Collaboration et al. 2022a) and their physical interpretation Akiyama & et al. (2019b); Kocherlakota et al. (2021); Event Horizon Telescope Collaboration et al. (2022b), we test the ability of the GRLBM in modelling the image of a black hole surrounded by a thin disc of matter emitting radiation. More specifically, we consider a Schwarzschild of mass  $M = 1$  and an infinitesimally thin disc with inner and outer edges at  $r_{\text{in}} = 6M$  and  $r_{\text{out}} = 12M$ , respectively. For simplicity, we assume the fluid to have zero velocity and set the energy density to unity everywhere in the disc and the flux density to zero apart from a thin layer above and below the disc, and keep them constant throughout the simulation. We then put an orthographic camera at  $(0, 0, -16)$  with a 10 degree tilt towards the disc, spanning the complete width and height of our numerical domain.

Figure 15 shows the lensed image of the thin disc when using 1454 directions and a fixed Lebedev stencil of order  $p_{\text{Leb}} = 65$ . While the image is obviously rather diffused since the orthographic camera only detects radiation passing orthogonally through the camera plane. While this test is not as efficient as the standard ray-tracing approach adopted to do black-hole imaging, and where the radiative-transfer

equation is solved along the photon geodesics (see, e.g., Gold & et al. 2020), it is quite remarkable that the GRLBM is able to reproduce the basic features of this lensed image, namely the intensity enhancement of the forward part of the disc (no Doppler boosting is possible because the fluid is assumed to have zero velocity), the lensing of the backward part of the disc, and even the lensed image of the lower sheet of the disc. Clearly, comparatively sharper images are possible when increasing the number of directions and the background grid resolution. In summary, the lensed thin-disc image represents a rather inexpensive test that the GRLBM passes successfully and that could be employed also in future implementations of general-relativistic treatments of the radiative-transfer problem.

### 5.3 Performance analysis

While in the previous sections we have clearly demonstrate the ability of the newly developed GRLBM to provide an accurate solution of the radiative-transfer equation in flat and curved spacetimes, we have not yet discussed the computational costs associated with the method and, in particular, how these costs vary when considering either a fixed stencil or an adaptive one. We recall that the tests have shown that the adaptive-streaming algorithm captures well the optically-thick regime and gives better results than the fixed-streaming method in the free-streaming regime, with the exception of the beam-crossing test where it is more diffusive. Given the higher computational costs of the adaptive approach, it is useful to measure how larger such costs are, both in flat and curved spacetimes.

Hence, we ran the code on a dual socket system with two Intel Xeon Silver 4314 CPUs with 32 cores running at 2.4 GHz each and measured the performance  $P$  in million lattice updates per second (MLUPS)

$$P = \frac{n_x n_y n_z n_t}{10^6 \tau_{\text{tot}}} \text{ MLUPS}. \quad (104)$$

The two scenarios considered are those of a vacuum with  $\kappa_0 = \kappa_1 = \kappa_a = \eta = u^i = 0$  and random initial moments  $E, F^i$ , together with that of a homogeneous fluid with  $\kappa_0 = 100, \kappa_1 = 20, \kappa_a = \eta = 10, u^x = 0.5$ , thus leading to four different benchmarks. For the GRLBM we use a Schwarzschild spacetime.

Figure 16 reports the results of these measurements showing, as in previous cases, the values for the 2D and 3D simulations on the left and right panels, respectively. When considering the performance of the SRLBM (left portions of each panel), the data both in 2D and 3D clearly indicates that the adaptive-stencil approach has a very high impact in the pure-streaming scenario in vacuum and leads to a significant speed-down. This is not the case when considering also the collisions, the difference between fixed and adaptive approaches being less pronounced because the collision step takes up a significant portion of the total runtime.

On the other hand, when looking at the GRLBM (right portions of each panel), all four benchmarks give similar results, thus indicating that the adaptive streaming has only a minor impact on the performance. This is because in this case also the fixed-streaming approach requires interpolations and these represent a good portion of the computational cost. Indeed, the addition of the collision step increases the total runtime only slightly. From these results, we conclude that adaptive-streaming is not particularly advantageous in generic scenarios investigated with the SRLBM, and that the additional computational costs are compensated only in regimes that are close to the free streaming. By contrast, the adaptive-streaming approach, which was specially designed for curved spacetimes, pro-

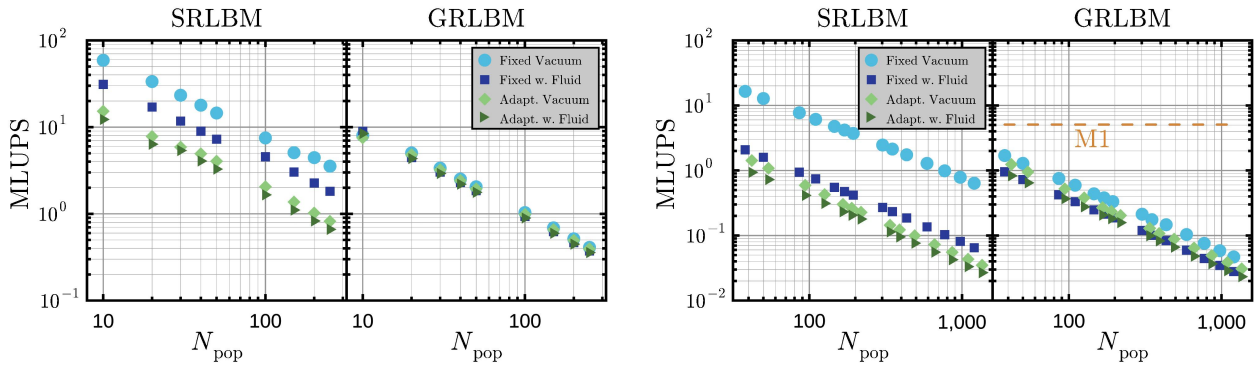


**Figure 16.** Performance analysis in terms of million lattice updates per second (MLUPS) and for four different scenarios: vacuum with  $\kappa_0 = \kappa_1 = \kappa_\alpha = \eta = u^i = 0$  and random initial moments  $E, F^i$ , and a homogeneous fluid with  $\kappa_0 = 100, \kappa_1 = 20, \kappa_\alpha = \eta = 10, u^x = 0.5$ . The left and right panels report the 2D and 3D data with  $400^2$  and  $100^3$  grid-points, respectively. In each case, the left and right columns report the results of the SRLBM and of the GRLBM. Each test is run ten times with  $n_t = 50$  and we report the best result for each configuration.

vides the optimal approach in all scenarios that could be of interest for the use of the GRLBM.

We conclude these considerations on the performance of the GRLBM by comparing its efficiency with that of the M1 scheme in the 3D scenarios. This is shown with a dashed horizontal line in the right portion of the right panel in Fig. 16, which highlights that the M1 approach always performs better than the GRLBM and that the additional costs can be even of two orders of magnitude larger in the case of large number of directions. While our GRLBM code is far from being optimised and its vectorisation with SIMD instructions could easily lead to a speed-up of a factor 10, it is unlikely that it will be less expensive than the M1 approach. Hence, and not differently from MonteCarlo approaches, the GRLBM should be seen as an appealing approach for a more accurate but also more expensive solution of the general-relativistic radiative-transfer equation.

## 6 CONCLUSION AND OUTLOOK

We have extended the special-relativistic lattice-Boltzmann method (SRLBM) for radiation transport by Weih et al. (2020c) to curved spacetimes, thus allowing for the solution of the radiative-transfer equation in curved spacetimes as those explored by GRMHD simulations of high-energy astrophysical phenomena. We recall that the lack of a closure relation is a significant advantage of the SRLBM for radiation transport over the M1 scheme Weih et al. (2020c). In particular, to compute the pressure tensor in the intermediate regime between optically thin and optically thick plasmas, moment-based approaches such as the M1 method, rely on the interpolation between closure relations in the optically thin and thick limits. The SRLBM, on the other hand, does not rely on any closure relation, as it allows for direct computation of any moment of the radiation field via the stencil quadrature.

The novel general-relativistic lattice-Boltzmann method (GRLBM) approach presented here is based on three main strategies:

(i) the streaming of carefully selected photons along null geodesics and interpolating their final positions, velocities, and frequency shifts to all photons in a given velocity stencil. Furthermore, in order to make the streaming along null geodesics numerically feasible, we introduce a spherical-harmonics extrapolation scheme, reducing the number of geodesic equations to solve drastically.

(ii) the use of transformation laws between the laboratory frame,

the Eulerian frame, and the fluid frame, enabling us to perform the collision step in the fluid frame, thus retaining the collision operator of the special-relativistic case with only minor modifications. As a result, we are able to model the evolution of the frequency-independent (“grey”) radiation field as it interacts with a background fluid via absorption, emission, and scattering in a curved background spacetime.

(iii) the introduction of an adaptive stencil, which is suitably distorted in the direction of propagation of the photon bundle, reduces the computational costs of the method while improving its performance in the optically-thin regime.

To verify the validity of the adaptive streaming scheme, we performed a series of tests in flat spacetime and compared them to fixed streaming, M1, and analytical solutions. We found that adaptive streaming gives the same results as fixed streaming in optically thick and intermediate regimes. In the free-streaming limit, adaptive streaming fixes the beam separation problem of fixed streaming but introduces more diffusion in beam crossing. The curved beam and the thin-disc test demonstrate the validity of the newly derived curved spacetime lattice-Boltzmann equations. The additional computational cost of adaptive streaming does not justify its usage in flat spacetime simulations unless one works on a memory-bound system. However, it has a negligible performance impact on the curved spacetime code, and we highly recommend using it in this context.

The discussion of the mathematical and numerical strategy developed for the GRLBM, and proposed here for the first time, is followed by the presentation of a series of standard and non-standard tests in 2D and 3D aimed at validating the correctness of the GRLBM under a variety of physical and numerical conditions. In all cases, we have demonstrated the ability of the GRLBM to provide an accurate solution of the general-relativistic radiative-transfer equation, thus opening the way to the use of the GRLBM in direct numerical simulations of astrophysical plasmas.

Overall, the results of the tests indicate that the adaptive-streaming approach is not particularly advantageous in generic scenarios investigated with the SRLBM, where the additional computational costs are not compensated but in those regimes that are close to the free streaming. By contrast, because it was specially designed for curved spacetimes, the adaptive-streaming provides the optimal method in all scenarios that could be of interest for the use of the GRLBM.

The results presented here are meant mostly as a proof-of-principle of the feasibility and robustness of the GRLBM approach. Hence,

much more can be done in future work to further optimise the techniques employed and increase the efficiency of the solution, e.g., by reducing the floating-point accuracy of the populations from 64 bit to 32 bit (which would also benefit GPU implementations), the use of the Voronoi interpolation in 3D for the velocity, or other less expensive quadratures on the two-sphere. However, given the intrinsically higher complexity of the approach, we regard the GRLBM as an appealing but also more expensive approach to the solution of the general-relativistic radiative-transfer equation. In this respect, the GRLBM is not dissimilar to equivalent Monte Carlo approaches, that are intrinsically more computationally intensive, although more accurate than the simpler moment-based approaches.

As a final remark, we note that the GRLBM could be used in combination with the M1 scheme in a way that is logically similar to the Guided-Moments approach suggested by Izquierdo et al. (2024). More specifically, the new scheme would use the M1 method in its standard form but replace the closure relation for the pressure tensor with a simplified GRLBM scheme that only computes the pressure tensor. We will explore this approach in future work.

## ACKNOWLEDGEMENTS

We thank C. Musolino, L. R. Weih, and S. Succi for helpful discussions and V. Lindenstruth for financial support. Support comes from the State of Hesse within the Research Cluster ELEMENTS (Project ID 500/10.006) and through the European Research Council Advanced Grant “JETSET: Launching, propagation and emission of relativistic jets from binary mergers and across mass scales” (grant No. 884631). LR acknowledges the Walter Greiner Gesellschaft zur Förderung der physikalischen Grundlagenforschung e.V. through the Carl W. Fueck Laureatus Chair.

## DATA AVAILABILITY

The corresponding author will share this paper’s data at a reasonable request.

## CODE AVAILABILITY

The 2D and 3D GRLBM codes developed for this work are freely accessible on github and can be found at <https://github.com/Tom-Olsen/2dRadiation> and <https://github.com/Tom-Olsen/3dRadiation>, respectively.

## REFERENCES

Akiyama K., et al. 2019a, *Astrophys. J. Lett.*, **875**, L1  
 Akiyama K., et al. 2019b, *Astrophys. J. Lett.*, **875**, L5  
 Bhatnagar P. L., Gross E. P., Krook M., 1954, *Phys. Rev.*, **94**, 511  
 Bobach T. A., 2009, PhD thesis, Technische Universität Kaiserslautern, [https://kluedo.ub.rptu.de/frontdoor/deliver/index/docId/2104/file/diss.bobach.natural\\_neighbor.20090615.pdf](https://kluedo.ub.rptu.de/frontdoor/deliver/index/docId/2104/file/diss.bobach.natural_neighbor.20090615.pdf)  
 Bovard L., Martin D., Guercilena F., Arcones A., Rezzolla L., Korobkin O., 2017, *Phys. Rev. D*, **96**, 124005  
 Chapman S., Cowling T. G., 1970, The mathematical theory of non-uniform gases. an account of the kinetic theory of viscosity, thermal conduction and diffusion in gases  
 Dietrich T., Ujevic M., 2017, *Classical and Quantum Gravity*, **34**, 105014

Espino P. L., Prakash A., Radice D., Logoteta D., 2024, *Phys. Rev. D*, **109**, 123009  
 Event Horizon Telescope Collaboration Akiyama K., et al., 2022a, *Astrophys. J. Lett.*, **930**, L12  
 Event Horizon Telescope Collaboration Akiyama K., et al., 2022b, *Astrophys. J. Lett.*, **930**, L17  
 Fernández R., Tchekhovskoy A., Quataert E., Foucart F., Kasen D., 2019, *Mon. Not. R. Astron. Soc.*, **482**, 3373  
 Foucart F., 2018, *Mon. Not. R. Astron. Soc.*, **475**, 4186  
 Foucart F., et al., 2015, *Phys. Rev. D*, **91**, 124021  
 Foucart F., Duez M. D., Hebert F., Kidder L. E., Pfeiffer H. P., Scheel M. A., 2020, *Astrophys. J. Lett.*, **902**, L27  
 Fujibayashi S., Kiuchi K., Nishimura N., Sekiguchi Y., Shibata M., 2018, *The Astrophysical Journal*, **860**, 64  
 Galeazzi F., Kastaun W., Rezzolla L., Font J. A., 2013, *Phys. Rev. D*, **88**, 064009  
 Gentle J. E., 2007, *Springer texts in statistics*, Springer, New York, NY, doi, **10**, 978  
 Gold R., et al. 2020, *Astrophys. J.*, **897**, 148  
 Higuera F. J., Succi S., Benzi R., 1989, *Europhysics Letters*, **9**, 345  
 Hubeny I., 2003, *Stellar Atmosphere Modeling*, 288, 17  
 Izquierdo M. R., Pareschi L., Miñano B., Massó J., Palenzuela C., 2022, *arXiv e-prints*, p. arXiv:2211.00027  
 Izquierdo M. R., Abalos F., Palenzuela C., 2024, *Phys. Rev. D*, **109**, 043044  
 Just O., Obergaulinger M., Janka H. T., 2015, *Mon. Not. R. Astron. Soc.*, **453**, 3386  
 Kent J. T., 1982, *Journal of the Royal Statistical Society: Series B (Methodological)*, **44**, 71  
 Kiuchi K., Sekiguchi Y., Kyutoku K., Shibata M., Taniguchi K., Wada T., 2015, *Phys. Rev. D*, **92**, 064034  
 Kocherlakota P., et al., 2021, *Phys. Rev. D*, **103**, 104047  
 Krüger T., Kusumaatmaja H., Kuzmin A., Shardt O., Silva G., Vigen E. M., 2017, The lattice Boltzmann method. Graduate Texts in Physics Vol. 10, Springer, doi:<https://doi.org/10.1007/978-3-319-44649-3>  
 Kuroda T., Takiwaki T., Kotake K., 2016, *Astrophys. J., Supp.*, **222**, 20  
 Melon Fuksman J. D., Mignone A., 2019, *Astrophys. J., Supp.*, **242**, 20  
 Mezzacappa A., Liebendörfer M., Messer O. E. B., Hix W. R., Thielemann F.-K., Bruenn S. W., 2001, *Phys. Rev. Lett.*, **86**, 1935  
 Misner C. W., Thorne K. S., Wheeler J. A., 1973, *Gravitation*. W. H. Freeman, San Francisco  
 Most E. R., Papenfort L. J., Rezzolla L., 2019, *Mon. Not. R. Astron. Soc.*, **490**, 3588  
 Müller T., Grave F., 2009, *arXiv preprint arXiv:0904.4184*  
 Musolino C., Rezzolla L., 2024, *Mon. Not. R. Astron. Soc.*, **528**, 5952  
 O’Connor E., 2015, *Astrophys. J., Supp.*, **219**, 24  
 Olivares H., Porth O., Davelaar J., Most E. R., Fromm C. M., Mizuno Y., Younsi Z., Rezzolla L., 2019, *Astron. Astrophys.*, **629**, A61  
 Palenzuela C., Lehner L., Ponce M., Liebling S. L., Anderson M., Neilsen D., Motl P., 2013, *Phys. Rev. Lett.*, **111**, 061105  
 Perego A., Radice D., Bernuzzi S., 2017, *Astrophys. J. Lett.*, **850**, L37  
 Pons J. A., Ibáñez J. M., Miralles J. A., 2000, *Mon. Not. R. Astron. Soc.*, **317**, 550  
 Porth O., Olivares H., Mizuno Y., Younsi Z., Rezzolla L., Moscibrodzka M., Falcke H., Kramer M., 2017, *Computational Astrophysics and Cosmology*, **4**, 1  
 Radice D., Abdikamalov E., Rezzolla L., Ott C. D., 2013, *Journal of Computational Physics*, **242**, 648  
 Radice D., Bernuzzi S., Perego A., Haas R., 2022, *Mon. Not. Roy. Astron. Soc.*, **512**, 1499  
 Rezzolla L., Miller J. C., 1994, *Class. Quantum Grav.*, **11**, 1815  
 Rezzolla L., Zanotti O., 2013, *Relativistic Hydrodynamics*. Oxford University Press, doi:10.1093/acprof:oso/9780198528906.001.0001  
 Rezzolla L., Giacomazzo B., Baiotti L., Granot J., Kouveliotou C., Aloy M. A., 2011, *Astrophys. J. Letters*, **732**, L6  
 Rosswog S., Korobkin O., Arcones A., Thielemann F.-K., Piran T., 2014, *Mon. Not. R. Astron. Soc.*, **439**, 744  
 Roth N., Anninos P., Robinson P. B., Peterson J. L., Polak B., Mangan T. K., Beyer K., 2022, *Astrophys. J.*, **933**, 226

- Ruffert M., Janka H.-T., Takahashi K., Schaefer G., 1997, *Astron. Astrophys.*, **319**, 122
- Siegel D. M., Ciolfi R., 2016, *Astrophys. J.*, **819**, 14
- Siegel D. M., Metzger B. D., 2017, *Phys. Rev. Lett.*, **119**, 231102
- Skinner M. A., Dolence J. C., Burrows A., Radice D., Vartanyan D., 2019, *Astrophys. J., Supp.*, **241**, 7
- Smit J. M., Cernohorsky J., Dullemond C. P., 1997, *Astron. Astrophys.*, **325**, 203
- Succi S., 2001, *The Lattice Boltzmann Equation for Fluid Dynamics and Beyond*. Clarendon Press, Oxford
- Sun L., Ruiz M., Shapiro S. L., Tsokaros A., 2022, *Phys. Rev. D*, **105**, 104028
- Vincent F. H., Gourgoulhon E., Novak J., 2012, *Classical and Quantum Gravity*, **29**, 245005
- Weih L. R., Hanauske M., Rezzolla L., 2020a, *Phys. Rev. Lett.*, **124**, 171103
- Weih L. R., Olivares H., Rezzolla L., 2020b, *Mon. Not. R. Astron. Soc.*, **495**, 2285
- Weih L. R., Gabbana A., Simeoni D., Rezzolla L., Succi S., Tripiccion R., 2020c, *Mon. Not. R. Astron. Soc.*, **498**, 3374

## APPENDIX A: LORENTZ TRANSFORMATIONS

Let  $\mathcal{A}$  and  $\mathcal{B}$  be two inertial frames and  $u^i$  the three-velocity of  $\mathcal{B}$  as measured by  $\mathcal{A}$ . The Lorentz factor and the Lorentz boost matrix are defined as,

$$\gamma = \frac{1}{\sqrt{1 - u_i u^i}}, \quad (\text{A1})$$

$$\Lambda^\mu{}_\nu = \begin{pmatrix} \gamma & -\gamma u_j \\ -\gamma u^i & \delta^i_j + (\gamma - 1)u^i u_j / u_k u^k \end{pmatrix}. \quad (\text{A2})$$

Let  $P^\mu = \nu N^\mu$  be a photon's four-momentum,  $\nu$  its frequency,  $N^\mu = (1, n^i)$  its four-velocity and  $n^i$  its three-velocity. By Lorentz boosting the time component of the four-momentum, we can derive the transformation law of the frequency,

$$\tilde{P}^0 = \tilde{\nu} \tilde{N}^0 = \Lambda^0{}_\mu P^\mu = \nu \Lambda^0{}_\mu N^\mu = \nu \left( \Lambda^0{}_0 N^0 + \Lambda^0{}_i N^i \right), \quad (\text{A3})$$

$$\Rightarrow \tilde{\nu} = \nu \gamma (1 - u_i n^i), \quad (\text{A4})$$

and by Lorentz boosting the spatial components of the four-momentum, we can derive the transformation law of the three-velocity,

$$\tilde{P}^i = \tilde{\nu} \tilde{N}^i = \Lambda^i{}_\mu P^\mu = \nu \left( \Lambda^i{}_0 N^0 + \Lambda^i{}_j N^j \right), \quad (\text{A5})$$

$$\Rightarrow \tilde{n}^i = \frac{\nu}{\tilde{\nu}} \left[ n^i - \left( 1 - \frac{\gamma u_j n^j}{\gamma + 1} \right) \gamma u^i \right]. \quad (\text{A6})$$

Through the principles of symmetry, we can immediately derive the inverse transformation laws, yielding the following results,

$$A = \gamma (1 - u_i n^i) = \frac{1}{\gamma (1 + u_i \tilde{n}^i)}, \quad (\text{A7})$$

$$\nu = \frac{\tilde{\nu}}{A}, \quad \tilde{\nu} = \frac{\nu}{A}, \quad (\text{A8})$$

$$n^i = A \left[ \tilde{n}^i + \left( 1 + \frac{\gamma u_j \tilde{n}^j}{\gamma + 1} \right) \gamma u^i \right], \quad (\text{A9})$$

$$\tilde{n}^i = \frac{1}{A} \left[ n^i - \left( 1 - \frac{\gamma u_j n^j}{\gamma + 1} \right) \gamma u^i \right], \quad (\text{A10})$$

where  $A$  is called the Doppler factor.

The specific intensity  $I_\nu$  is the energy  $dE_\nu$  per time  $dt$ , area  $d^{D-1}x$ , frequency  $d\nu$ , and solid angle  $d\Omega$ , or simply the 'energy per everything',

$$I_\nu = \frac{dE_\nu}{dt d^{D-1}x d\nu d\Omega}, \quad (\text{A11})$$

$$dE_\nu = \nu dN, \quad (\text{A12})$$

$$dN = f d^D r d^D p, \quad (\text{A13})$$

$$d^D p = p^{D-1} dp d\Omega = \nu^{D-1} d\nu d\Omega, \quad (\text{A14})$$

$$d^D r = dt d^{D-1}x. \quad (\text{A15})$$

The letter  $D$  denotes the dimensionality of space,  $N$  is the number of photons we are looking at, and  $f$  is the Lorentz invariant phase space density of photons. Putting everything together we get,

$$I_\nu = \nu^D f. \quad (\text{A16})$$

We already know how the frequency transforms and that the phase space density is Lorentz invariant. From this, we can directly derive the transformation law of the specific intensity, which is dimension-dependent,

$$I_\nu = \frac{\tilde{I}_{\tilde{\nu}}}{A^D}, \quad \tilde{I}_{\tilde{\nu}} = I_\nu A^D. \quad (\text{A17})$$

The transformation law of the 'grey' or total intensity directly follows as,

$$I = \int_0^\infty I_\nu d\nu \Rightarrow I = \frac{\tilde{I}}{A^{D+1}}, \quad \tilde{I} = IA^{D+1}. \quad (\text{A18})$$

The last transformation law we need is that of the solid angle  $d\Omega$ . For this, we take a close look at the following invariant Lorentz scalar,

$$e = u_\mu u_\nu T^{\mu\nu} = \oint_S \underbrace{u_\mu u_\nu p^\mu p^\nu}_a \frac{I d\Omega}{v^2}. \quad (\text{A19})$$

The factor  $a$  is invariant because it is a full contraction and, therefore, a Lorentz scalar. This means that the factor  $b$  must also be invariant. However, we already know how the total intensity  $I$  and the frequency  $\nu$  transform. Therefore, the solid angle  $d\Omega$  must transform as,

$$d\Omega = d\tilde{\Omega} A^{D-1}, \quad d\tilde{\Omega} = \frac{d\Omega}{A^{D-1}}. \quad (\text{A20})$$

## APPENDIX B: COLLISION OPERATOR

The most general representation of the Lorentz-invariant collision operator in Eq. (34) is given by,

$$\Gamma[f_\nu] = \oint_{4\pi} \int_0^\infty \nu'^3 [f'_{\nu'}(1 - f_\nu)R^I - f_\nu(1 - f'_{\nu'})R^O] d\nu' d\Omega'. \quad (\text{B1})$$

The incoming and outgoing scattering kernels,  $R^I = R^I(\nu, \nu', n^i, n'^i)$  and  $R^O = R^O(\nu, \nu', n^i, n'^i)$ , depend on the underlying scattering model, which is usually expressed in the fluid frame, where the scattering center rests. By assuming iso-energetic scattering, we can neglect the frequency dependence of the scattering kernels and expand them in a Legendre series,

$$\tilde{R}(\tilde{\nu}, \tilde{\nu}', \tilde{n}^i, \tilde{n}'^i) = \tilde{R}^I(\tilde{\nu}, \tilde{\nu}', \tilde{n}^i, \tilde{n}'^i) = \tilde{R}^O(\tilde{\nu}, \tilde{\nu}', \tilde{n}^i, \tilde{n}'^i) \quad (\text{B2})$$

$$\approx \left(\frac{1}{2}\tilde{\Phi}_0 + \frac{3}{2}\tilde{\Phi}_1 \tilde{n}_i \tilde{n}'^i\right) \delta(\tilde{\nu} - \tilde{\nu}'). \quad (\text{B3})$$

We then define the scattering opacities in terms of the Legendre coefficients,  $\tilde{\kappa}_{I,\tilde{\nu}} = 2\pi \tilde{\nu}^2 \tilde{\Phi}_I$ . The collision operator in the fluid frame then becomes,

$$\tilde{\Gamma}[f_{\tilde{\nu}}] = \oint_{4\pi} \int_0^\infty \tilde{\nu}'^3 (f'_{\tilde{\nu}'} - f_{\tilde{\nu}}) \tilde{R} d\tilde{\nu}' d\tilde{\Omega}' \quad (\text{B4})$$

$$= \oint_{4\pi} \tilde{\nu}'^3 (f'_{\tilde{\nu}'} - f_{\tilde{\nu}}) \left(\frac{1}{2}\tilde{\Phi}_0 + \frac{3}{2}\tilde{\Phi}_1 \tilde{n}_i \tilde{n}'^i\right) d\tilde{\Omega}' \quad (\text{B5})$$

$$= \frac{\tilde{\nu}}{4\pi} \oint_{4\pi} (f'_{\tilde{\nu}'} - f_{\tilde{\nu}}) (\tilde{\kappa}_{0,\tilde{\nu}} + 3\tilde{\kappa}_{1,\tilde{\nu}} \tilde{n}_i \tilde{n}'^i) d\tilde{\Omega}' \quad (\text{B6})$$

$$= \tilde{\nu} [\tilde{\kappa}_{0,\tilde{\nu}} (\tilde{E}_{\tilde{\nu}} - f_{\tilde{\nu}}) + 3\tilde{\kappa}_{1,\tilde{\nu}} \tilde{n}_i \tilde{F}_{\tilde{\nu}}^i], \quad (\text{B7})$$

where we have used the monochromatic radiation moments,

$$E_\nu = \frac{1}{4\pi} \oint_{4\pi} f_\nu d\Omega, \quad (\text{B8})$$

$$F_\nu^i = \frac{1}{4\pi} \oint_{4\pi} f_\nu n^i d\Omega. \quad (\text{B9})$$

Note that the final form of our collision operator in Eq. (B7) is not Lorentz-invariant anymore and thus only valid in the fluid frame.

## APPENDIX C: TETRAD SEPARATION

For our curved spacetime LBM scheme, we need a tetrad to transform any tensors between the LF and the EF. The tetrad  $e$  must then obey,

$$\eta_{\tilde{\mu}\tilde{\nu}} = g_{\mu\nu} e^\mu_{\tilde{\mu}} e^\nu_{\tilde{\nu}} \Leftrightarrow \eta = e^T g e. \quad (\text{C1})$$

Due to the symmetry of  $g_{\mu\nu}$  and  $\eta_{\tilde{\mu}\tilde{\nu}}$  Equation (C1) contains only 10 unique equations, but 16 unknowns. The missing six constraints correspond to the six degrees of freedom of the Lorentz group, consisting of three spatial rotations and three velocity boosts. This can be shown by boosting Eq. (C1) with two boost matrices,

$$\eta_{\tilde{\mu}\tilde{\nu}} \Lambda^{\tilde{\mu}}_{\tilde{\alpha}} \Lambda^{\tilde{\nu}}_{\tilde{\beta}} = g_{\mu\nu} e^\mu_{\tilde{\mu}} \Lambda^{\tilde{\mu}}_{\tilde{\alpha}} e^\nu_{\tilde{\nu}} \Lambda^{\tilde{\nu}}_{\tilde{\beta}}, \quad (\text{C2})$$

$$\Rightarrow \eta_{\tilde{\alpha}\tilde{\beta}} = g_{\mu\nu} \underbrace{e^\mu_{\tilde{\mu}} \Lambda^{\tilde{\mu}}_{\tilde{\alpha}}}_{b^\mu_{\tilde{\alpha}}} \underbrace{e^\nu_{\tilde{\nu}} \Lambda^{\tilde{\nu}}_{\tilde{\beta}}}_{b^\nu_{\tilde{\beta}}}. \quad (\text{C3})$$

The invariance of the Minkowski metric leaves it unchanged under Lorentz-transformations  $\Lambda^{\tilde{\mu}}_{\tilde{\alpha}}$ . Thus, the boosted tensor  $b^\mu_{\tilde{\alpha}} = e^\mu_{\tilde{\mu}} \Lambda^{\tilde{\mu}}_{\tilde{\alpha}}$  also obeys Eq. (C1) and is, therefore, a valid tetrad.

While in most cases, we are not interested in the exact spatial orientation of the IF, the boost of the IF is important. We can read the boost of the IF directly from the tetrad by comparing the first column of the tetrad to the four-velocity of the IF. Let  $u^\mu$  be the four-velocity of the IF as seen in the LF. The IF sees itself being at rest in its frame of reference,  $\tilde{u}^\mu = (1, \tilde{0}^k)$ . Transforming the four-velocity between these two reference frames then yields,

$$u^\mu = e^\mu_{\tilde{\nu}} \tilde{u}^\nu = e^\mu_0 \tilde{u}^0 + e^\mu_i \tilde{u}^i = e^\mu_0 1 + e^\mu_i 0^i = e^\mu_0. \quad (\text{C4})$$

The fundamental ansatz of the tetrad separation is to constraint the tetrad to a lower triangular matrix and then split it into four separate tensors

$$e = (e^\mu_{\tilde{\nu}}) = \begin{pmatrix} e^0_0 & 0 & 0 & 0 \\ e^1_0 & e^1_1 & 0 & 0 \\ e^2_0 & e^2_1 & e^2_2 & 0 \\ e^3_0 & e^3_1 & e^3_2 & e^3_3 \end{pmatrix} = ABCD, \quad (\text{C5})$$

$$A = \begin{pmatrix} e^0_0 & 0 & 0 & 0 \\ e^1_0 & 1 & 0 & 0 \\ e^2_0 & 0 & 1 & 0 \\ e^3_0 & 0 & 0 & 1 \end{pmatrix}, \quad B = \begin{pmatrix} 1 & 0 & 0 & 0 \\ 0 & e^1_1 & 0 & 0 \\ 0 & e^2_1 & 1 & 0 \\ 0 & e^3_1 & 0 & 1 \end{pmatrix},$$

$$C = \begin{pmatrix} 1 & 0 & 0 & 0 \\ 0 & 1 & 0 & 0 \\ 0 & 0 & e^2_2 & 0 \\ 0 & 0 & e^3_2 & 1 \end{pmatrix}, \quad D = \begin{pmatrix} 1 & 0 & 0 & 0 \\ 0 & 1 & 0 & 0 \\ 0 & 0 & 1 & 0 \\ 0 & 0 & 0 & e^3_3 \end{pmatrix}.$$

The six zeroes fix the six degrees of freedom of the Lorentz group, meaning that our final tetrad spatial orientation and boost are already determined.

Inserting the separation ansatz into the matrix representation of Eq. (C1) allows us to write it in an iterative manner

$$\eta = e^T g e = D^T C^T B^T A^T g^0 ABCD \quad (\text{C6})$$

$$= D^T C^T B^T g^1 BCD \quad (\text{C7})$$

$$= D^T C^T g^2 CD \quad (\text{C8})$$

$$= D^T g^3 D = g^4. \quad (\text{C9})$$

Going back to index notation and taking a closer look at the first step,  $g^1 = A^T g^0 A$ , we can see that it only affects the first column and row

of the resulting intermediate matrix,

$$g_{\mu\nu}^1 = g_{\alpha\beta}^0 A^\alpha_\mu A^\beta_\nu, \quad (\text{C10})$$

$$g_{ij}^1 = g_{\alpha\beta}^0 A^\alpha_i A^\beta_j = g_{00}^0 A^0_i A^0_j + 2g_{0k}^0 A^0_i A^k_j + g_{ab}^0 A^a_i A^b_j \\ = g_{00}^0 \cdot 0 \cdot 0 + 2g_{0k}^0 \cdot 0 \cdot A^k_j + g_{ab}^0 \delta^a_i \delta^b_j = g_{ij}^0, \quad (\text{C11})$$

$$g_{0i}^1 = g_{\alpha\beta}^0 A^\alpha_0 A^\beta_i = A_{\beta 0} A^\beta_i = A_{00} A^0_i + A_{j0} A^j_i \\ = A_{00} \cdot 0 + A_{j0} \delta^j_i = A_{i0} \stackrel{!}{=} 0_i, \quad (\text{C12})$$

$$g_{00}^1 = g_{\alpha\beta}^0 A^\alpha_0 A^\beta_0 = A_{\beta 0} A^\beta_0 \stackrel{!}{=} -1. \quad (\text{C13})$$

Furthermore, we can conclude from Eq. (C13) that the column four-vector  $A^\mu_0$  in  $\mathbf{A}$  must be timelike. Eq. (C12) tells us that the covariant spatial components of  $A_{\mu 0}$  must vanish, meaning that it is orthogonal to a three-dimensional hypersurface of constant coordinate time. For any metric, there only is one such future-directed four-vector, the four-velocity of the Eulerian observer,

$$A^\mu_0 = n^\mu = \frac{1}{\alpha} (1, -\beta^i), \quad n_\mu = (-\alpha, 0_i). \quad (\text{C14})$$

The resulting intermediate tensor  $\mathbf{g}^1$  now takes the form,

$$\mathbf{g}^1 = \begin{pmatrix} -1 & 0_j \\ 0_i & g_{ij} \end{pmatrix}, \quad (\text{C15})$$

meaning we successfully ‘‘diagonalised’’ the first row and column.

Due to the nature of our split, the following iterations will not alter the diagonalised part from the previous iteration. To continue we repeat the calculations in (C10) to (C13) but for  $\mathbf{g}^2 = \mathbf{B}^T \mathbf{g}^1 \mathbf{B}$ . In the following, we introduce capitalised indices, which run from two to three,  $I, J, K \in \{2, 3\}$ .

$$g_{ij}^2 = g_{ab}^1 B^a_i B^b_j, \quad (\text{C16})$$

$$g_{IJ}^2 = g_{ab}^1 B^a_I B^b_J = g_{11}^1 B^1_I B^1_J + 2g_{1K}^1 B^1_I B^K_J + g_{AB}^1 B^A_I B^B_J \\ = g_{11}^1 \times 0 \times 0 + 2g_{1K}^1 \times 0 \times B^K_J + g_{AB}^1 \delta^A_I \delta^B_J = g_{IJ}^1, \quad (\text{C17})$$

$$g_{I1}^2 = g_{ab}^1 B^a_I B^b_1 = B_{b1} B^b_I = B_{11} B^1_I + B_{J1} B^J_I \\ = B_{11} \times 0 + B_{J1} \delta^J_I = B_{I1} \stackrel{!}{=} 0_I, \quad (\text{C18})$$

$$g_{11}^2 = g_{ab}^1 B^a_1 B^b_1 = B_{b1} B^b_1 \stackrel{!}{=} 1. \quad (\text{C19})$$

In contrast to the previous iteration the three-vector  $B^i_1$  in  $\mathbf{B}$  must now be spacelike instead of timelike, while still having a vanishing contravariant part in the last two components. We introduce an Euclidean 2 + 1-split inspired by the 3 + 1-formalism to construct a vector with precisely these properties,

$$\tilde{g}_{ij} = \begin{pmatrix} \tilde{\alpha}^2 + \tilde{\beta}_K \tilde{\beta}^K & -\tilde{\beta}_j \\ -\tilde{\beta}_I & \tilde{\gamma}_{IJ} \end{pmatrix}, \quad (\text{C20})$$

$$\tilde{g}^{ij} = \begin{pmatrix} 1/\tilde{\alpha}^2 & \tilde{\beta}^j/\tilde{\alpha}^2 \\ \tilde{\beta}^I/\tilde{\alpha}^2 & \tilde{\gamma}^{IJ} + \tilde{\beta}^I \tilde{\beta}^J/\tilde{\alpha}^2 \end{pmatrix}, \quad (\text{C21})$$

$$\tilde{\gamma}_{IJ} = \tilde{g}_{IJ}, \quad \tilde{\gamma}^{IJ} = (\tilde{\gamma}_{IJ})^{-1} = \tilde{g}^{IJ} - \tilde{\beta}^I \tilde{\beta}^J/\tilde{\alpha}^2, \quad (\text{C22})$$

$$\tilde{\beta}_I = -\tilde{g}_{I1}, \quad \tilde{\beta}^I = \tilde{\gamma}^{IJ} \tilde{\beta}_J = \tilde{\alpha}^2 \tilde{g}^{I1}, \quad (\text{C23})$$

$$\tilde{\alpha} = \frac{1}{\sqrt{\tilde{g}^{11}}} = \sqrt{\tilde{g}_{11} - \tilde{\beta}_I \tilde{\beta}^I}, \quad (\text{C24})$$

$$\tilde{n}_i = (\tilde{\alpha}, 0_I), \quad \tilde{n}^i = \frac{1}{\tilde{\alpha}} (1, \tilde{\beta}^I)^T, \quad \tilde{n}_i \tilde{n}^i = 1. \quad (\text{C25})$$

We mark all 2 + 1-split quantities with a tilde to differentiate between the two splits. By construction, the three-vector  $\tilde{n}^i$  has precisely the properties we are looking for, giving us the solution for the tensor  $\mathbf{B}$ ,

$$B^i_1 = \tilde{n}^i = \frac{1}{\tilde{\alpha}} (1, \tilde{\beta}^I), \quad \tilde{n}_i = (\tilde{\alpha}, 0_I). \quad (\text{C26})$$

For the tensor  $\mathbf{C}$ , we repeat the procedure with an even simpler 1 + 1-split, and the final tensor  $\mathbf{D}$  follows trivially. We leave this exercise for the interested reader. We present the final solution in terms of the 3 + 1-components and the original metric.

$$A^\mu_0 = e^\mu_{\bar{0}} = n^\mu = \frac{1}{\alpha} (1, -\beta^i)^T, \quad (\text{C27})$$

$$B^i_1 = e^i_{\bar{1}} = \tilde{n}^i = \frac{1}{\tilde{\alpha}} (1, \tilde{\beta}^I)^T, \quad (\text{C28})$$

$$C^I_2 = e^I_{\bar{2}} = \frac{1}{A} (1, B), \quad (\text{C29})$$

$$D^3_3 = e^3_{\bar{3}} = \frac{1}{\sqrt{g_{33}}}. \quad (\text{C30})$$

The four-velocity of the Eulerian observer is well known, and the other components are given by,

$$\tilde{\alpha} = \sqrt{g_{11} + \frac{(g_{12})^2 g_{33} + (g_{13})^2 g_{22} - 2g_{12} g_{13} g_{23}}{(g_{23})^2 - g_{22} g_{33}}}, \quad (\text{C31})$$

$$\tilde{\beta}^I = \frac{1}{(g_{23})^2 - g_{22} g_{33}} \begin{pmatrix} g_{12} g_{33} - g_{13} g_{23} \\ g_{13} g_{22} - g_{12} g_{23} \end{pmatrix}, \quad (\text{C32})$$

$$A = \sqrt{g_{22} - \frac{(g_{23})^2}{g_{33}}}, \quad (\text{C33})$$

$$B = -\frac{g_{23}}{g_{33}}. \quad (\text{C34})$$

The resulting tetrad from this procedure is always comoving with the Eulerian observer. As usual, it can be boosted to obtain any other tetrad. For example, in order to obtain a stationary tetrad  $\tilde{e}^\mu_\nu$ , the boost matrix would be constructed as follows

$$\Lambda^\mu_\nu = \begin{pmatrix} \gamma & -\gamma u_j \\ -\gamma u^i & \delta^i_j + (\gamma - 1) u^i u_j / u^k u_k \end{pmatrix}, \quad (\text{C35})$$

$$e^0_0 = \frac{1}{\sqrt{-g_{00}}} = e^0_\alpha \Lambda^\alpha_0 = e^0_0 \gamma \Rightarrow \gamma = \frac{1}{e^0_0 \sqrt{-g_{00}}}, \quad (\text{C36})$$

$$\tilde{e}^i_0 = 0^i = e^i_\alpha \Lambda^\alpha_0 = \gamma (n^i - e^i_j u^j) \Rightarrow u^j = e^j_i n^i. \quad (\text{C37})$$

Note that the inverse tetrad  $e_\mu^\nu$  and sub-tetrad  $e_i^j$  are easy to compute due to the lower triangular nature of our ansatz.

Finally, we compare the performance of our new approach to the Gramm-Schmidt process (Gentle 2007). We use the following setup for the performance comparison to simulate a realistic scenario similar to GRMHD simulations. We initialise a metric and pre-compute the corresponding 3 + 1-components on a numerical Cartesian grid of  $200 \times 200 \times 200$  points. For the metric, we use a Cartesian Kerr-Schild metric with  $M = 1$  and  $a = 0.5$ , ensuring that no metric components are zero. We then calculate a tetrad on each grid cell for both codes on a single core and measure the run time 1000 times for statistics. Tab. C1 shows the results for four different cases. The stationary and comoving Gramm-Schmidt solutions only differ in the choice of the first seed vector,  $s^0_0 = (1, 0^i)$  vs.  $s^0_0 = n^\mu$ , and are therefore almost identical. The stationary and comoving tetrad separation solutions differ in the additional Lorentz boost. For this, we need to invert the lower triangular three-by-three matrix  $e^i_j$ , which adds a noticeable amount of time but still outperforms the Gramm-Schmidt method.

Comparing the two methods, we get a speedup of 1.58 for the stationary case and 12.59 for the comoving tetrad when using the tetrad separation algorithm. The comoving tetrad is more desirable for our use case, making this new method ideal for constructing tetrads.

	GS st.	GS com.	Sep st.	Sep com.
Average[ms]	789.2	803.8	509.3	62.7
Max[ms]	795.7	812.9	514.0	67.7
Min[ms]	784.8	799.1	501.2	61.2
Std dev[ms]	2.3	2.5	2.6	2.1

**Table C1.** Gramm-Schmidt (GS) and Tetrad-Separation (Sep) run times for stationary (st.) and comoving (com.) tetrads.

## APPENDIX D: INITIAL DATA

The initial data is given as energy and flux density in the LF,  $E_{\text{ID}}$ ,  $F_{\text{ID}}^i$ , for every grid point. To convert these into initial data for the individual intensities, we first convert them to the local IF,  $\bar{E}_{\text{ID}}$ ,  $\bar{F}_{\text{ID}}^i$ . There does not exist a unique mapping from the IF energy and flux density to the intensity distribution. As an ansatz, we use the Kent distribution (Kent 1982) with the normalized flux direction  $\vec{e}_F$  as its direction vector.

$$\vec{e}_F = \vec{\bar{F}}_{\text{ID}} / |\vec{\bar{F}}_{\text{ID}}|, \quad (\text{D1})$$

$$I(\theta) = \bar{E}_{\text{ID}} \exp[\sigma \vec{e}_F \vec{n}(\theta) - A] = \bar{E}_{\text{ID}} \exp[\sigma \cos \theta - A]. \quad (\text{D2})$$

Without loss of generality, we can compute the moment integrals in a spherical coordinate system that is aligned with the flux direction, meaning  $\vec{e}_F$  is parallel to  $\vec{e}_z$  the upward pointing unit vector

$$\bar{E}_{\text{ID}} = \frac{1}{4\pi} \int_0^{2\pi} \int_0^\pi I(\theta) \sin \theta d\theta d\phi \quad (\text{D3})$$

$$= \frac{\bar{E}_{\text{ID}}}{2} \int_0^\pi \exp[\sigma \cos \theta - A] \sin \theta d\theta \quad (\text{D4})$$

$$= \bar{E}_{\text{ID}} \exp[-A] \frac{\sinh(\sigma)}{\sigma}, \quad (\text{D5})$$

from which we deduce

$$A = \ln \left( \frac{\sinh(\sigma)}{\sigma} \right), \quad (\text{D6})$$

$$\bar{F}_{\text{ID}}^z = \frac{1}{4\pi} \int_0^{2\pi} \int_0^\pi I(\theta) \cos \theta \sin \theta d\theta d\phi \quad (\text{D7})$$

$$= \frac{\bar{E}_{\text{ID}}}{2} \int_0^\pi \exp[\sigma \cos \theta - A] \cos \theta \sin \theta d\theta \quad (\text{D8})$$

$$= \frac{\bar{E}_{\text{ID}}}{\sigma^2} (\sigma \cosh \sigma - \sinh \sigma), \quad (\text{D9})$$

so that

$$\bar{F}_{\text{ID}}^z = \frac{\bar{E}_{\text{ID}}}{\sinh \sigma} \frac{\sigma \cosh \sigma - \sinh \sigma}{\sigma}. \quad (\text{D10})$$

The variable  $A$  scales the distribution to the given energy density and can be determined analytically if  $\sigma$  is known. The variable  $\sigma$  determines how narrow the distribution is and, therefore, the flux density. We are interested in a function for  $\sigma(|\vec{F}_{\text{ID}}^z|/\bar{E}_{\text{ID}})$ , but Eq. (D10) is not analytically invertible. However, it is strictly monotonically growing and, therefore, straightforward to invert numerically using a lookup table.

While the Kent distribution allows us to map a given energy and flux density to an intensity population distribution, it does not give us control over the pressure density  $P^{ij}$ . With the above approach, the pressure tensor will always be diagonal in the coordinate system aligned with the flux density. To be more precise, the pressure tensor

$N_{\text{real}} + N_{\text{ghost}}$	Flux max	$N_{\text{real}} + N_{\text{ghost}}$	Flux max
20 + 0	0.911348	16 + 4	0.980785
50 + 0	0.989806	40 + 10	0.995807
100 + 0	0.995896	80 + 20	0.998677
200 + 0	0.998210	160 + 40	0.999231

**Table D1.** Maximal achievable relative flux density for multiple Fourier stencils (2D) with different direction configurations. The last three columns show the respective population counts.

$p$	0.00 - 0.00	0.15 - 0.00	0.00 - 0.15	$N_{\text{dir}}$	$N_{\text{dir}}$	$N_{\text{dir}}$
11	0.119301	0.320176	0.401914	50	54	58
15	0.151213	0.407415	0.491836	86	94	102
17	0.260644	0.614494	0.687429	110	126	138
19	0.300239	0.657584	0.724383	146	166	182
21	0.305549	0.627482	0.743574	170	190	206
23	0.421269	0.782529	0.833982	194	218	238
29	0.586264	0.870299	0.906942	302	338	362
31	0.490054	0.808158	0.865103	350	390	422
35	0.707619	0.920281	0.948240	434	490	526
41	0.791457	0.953830	0.970163	590	662	710
47	0.846724	0.970273	0.975960	770	862	918

**Table D2.** Maximal achievable relative flux density for multiple Lebedev stencils (3D) of order  $p$ . The last three columns show the respective population counts.

in the aligned system is given by

$$P^{xx} = \frac{\bar{E}_{\text{ID}}}{4\pi} \int_0^{2\pi} \int_0^\pi \exp[\sigma \cos \theta - A] (\sin \theta \cos \phi)^2 \sin \theta n^i n^j d\theta d\phi$$

$$= \frac{\bar{E}_{\text{ID}}}{\sigma^2 \sinh \sigma} (\sigma \cosh(\sigma) - \sinh(\sigma)), \quad (\text{D11})$$

$$P^{yy} = \frac{\bar{E}_{\text{ID}}}{4\pi} \int_0^{2\pi} \int_0^\pi \exp[\sigma \cos \theta - A] (\sin \theta \sin \phi)^2 \sin \theta n^i n^j d\theta d\phi$$

$$= \frac{\bar{E}_{\text{ID}}}{\sigma^2 \sinh \sigma} (\sigma \cosh(\sigma) - \sinh(\sigma)), \quad (\text{D12})$$

$$P^{zz} = \frac{\bar{E}_{\text{ID}}}{4\pi} \int_0^{2\pi} \int_0^\pi \exp[\sigma \cos \theta - A] (\cos \theta)^2 \sin \theta n^i n^j d\theta d\phi$$

$$= \frac{\bar{E}_{\text{ID}}}{\sigma^2 \sinh \sigma} ((\sigma^2 + 2) \sinh(\sigma) - 2\sigma \cosh(\sigma)). \quad (\text{D13})$$

Not all energy and flux density combinations can be achieved depending on the chosen stencil. Each stencil has a maximum  $\sigma_{\text{max}}$  it can handle, depending on the population count  $N_{\text{dir}}$  and the additional ghost directions. Once  $\sigma$  exceeds  $\sigma_{\text{max}}$ , the distribution will be too sharp to be resolved by the stencil and seem discontinuous. This leads to errors in the velocity interpolation becoming too big. To find this  $\sigma_{\text{max}}$  value, we calculate the Kent distribution for  $\sigma = 1$ . We then interpolate the intensity to a grid of  $100 \times 200$  points in the region  $0.1\pi$  around the north pole of the stencil. If the relative maximal interpolation error does not exceed 1%, the current  $\sigma$  value is acceptable, and we increase  $\sigma$  by an adaptive stepsize. Otherwise, we repeat the process with a smaller stepsize until we have reached a reasonable estimate for the maximal allowed  $\sigma$ . As a result, there is a maximum relative flux density  $\bar{F}_i \bar{F}^i / \bar{E} \leq 1$  a stencil can resolve. Tables D1 and D2 show the maximum relative flux density for multiple Fourier and Lebedev stencils with different orders and refinement levels.

Adaptive stencils achieve better results in beam tests even with a

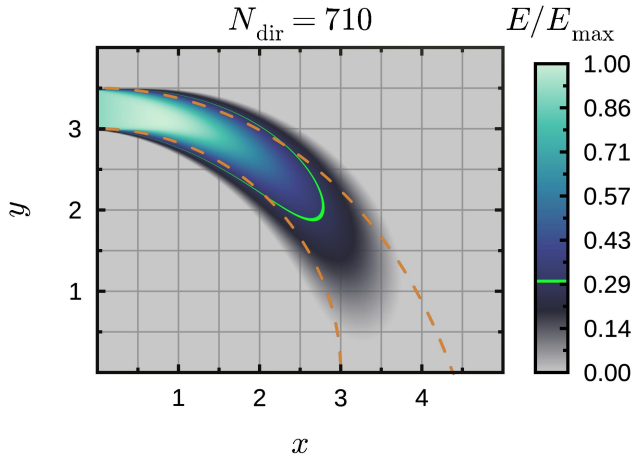


**Figure D1.** Normalised energy density for the 3D curved-beam test (see also Fig 14) with maximal interpolation error of 5% instead of 1%, resulting in  $\sigma_{\max} = 84.75$  instead of  $\sigma_{\max} = 33.52$ . The beam reaches its maximum energy density along its path instead of the very beginning, which is unphysical.

lower  $N_{\text{dir}}$  because they can achieve higher relative flux values with fewer direction vectors. This is achieved by increasing the resolution in the flux direction instead of homogeneously all around the sphere.

In Fig. D1, it is possible to note the effect of a  $\sigma > \sigma_{\max}$  on a curved beam test. The energy density along the beam increases and reaches its maximum in the middle of the beam instead of the beginning. The maximum relative flux limitation is only relevant in cases where the radiation field becomes highly focused and traverses mono-directional, which might be an issue in some extreme cases, e.g., a black-hole jet emissions.

This paper has been typeset from a  $\text{\TeX}/\text{\LaTeX}$  file prepared by the author.